Spectroscopic Study of $[Fe_2(O_2)(OBz)_2\{HB(pz')_3\}_2]$: Nature of the μ-1,2 Peroxide−Fe(III) Bond and Its Possible Relevance to O_2 Activation by Non-Heme Iron Enzymes

Thomas C. Brunold,[†] Nobuchika Tamura,[‡] Nobumasa Kitajima,[‡] Yoshihiko Moro-oka,[‡] and Edward I. Solomon*,[†]

Contribution from the Department of Chemistry, Stanford University, Stanford, California, 94305, and the Research Laboratory of Resources Utilization, Tokyo Institute of Technology, 4259 Nagatsuta, Yokohama 227, Japan

Received January 12, 1998

Abstract: Spectroscopic and theoretical studies of a binuclear cis μ-1,2 peroxide-bridged Fe(III) complex, $[Fe_2(O_2)(OBz)_2\{HB(pz')_3\}_2]$, where $HB(pz')_3$ represents hydrotris(3,5-diisopropyl-1-pyrazolyl)borate and OBz is benzoate, are presented and discussed. It is shown that the high O−O stretching frequency of 876 cm^{-1} does not reflect a strong O−O bond (k_{O-O} = 3.1 mdyn/Å) but rather results from substantial mechanical coupling between the Fe−O and O−O stretch motions. The coupling strength in μ-1,2 peroxide-bridged complexes is mainly determined by the metal−O−O bond angle, and this angle is larger in the three structurally characterized Fe−peroxide dimers than in related Cu and Co dimers due to a strong π-bonding interaction in the former. Using absorption, magnetic circular dichroism, and resonance Raman spectroscopies we can identify four peroxide-to-Fe charge transfer (CT) transitions contributing to the optical absorption spectrum below 35 000 cm^{-1}. These transitions give rise to two similarly intense bands centered at ∼14 600 and 26 200 cm^{-1} ($\epsilon \sim 3800$ M^{-1} cm^{-1}) and to weaker features at 12 500 cm^{-1} (∼400 M^{-1} cm^{-1}) and 24 650 cm^{-1} (∼1600 M^{-1} cm^{-1}). A complete band assignment based on the experimental data and assisted by density functional calculations is presented and provides significant insight into Fe−peroxide bonding. From a quantitative analysis of the optical absorption and resonance Raman data within the framework of time-dependent theory of electronic spectroscopy it follows that the π contribution to the peroxide → Fe charge donation amounts to 50−65%. The σ contribution, however, is smaller than in the well-characterized trans μ-1,2 peroxide-bridged Cu(II) dimer, and the charge on peroxide is thus similar in the two complexes, suggesting that the bridging peroxide in $[Fe_2(O_2)(OBz)_2\{HB(pz')_3\}_2]$ has a rather basic/nucleophilic character. The mechanistic implications of these results for the conversion of the putative cis μ-1,2 peroxide-bridged diiron(III) intermediate (P or H_{peroxo}) of methane monooxygenase to a high-valent diiron(IV)−oxo species are discussed.

Introduction

Dioxygen binding and activation for further reactions are key processes in biological systems carried out by a number of metalloproteins. In addition to the well-studied hemoproteins,[1] a class of proteins participating in these processes with carboxylate-bridged binuclear non-heme iron active sites has received much interest in the past decade.[2,3] The diversity of dioxygen-dependent reactions carried out by this class of proteins parallels that known for hemoproteins. Reversible dioxygen binding to the diferrous active site of hemerythrin (Hr), a dioxygen carrier protein in invertebrates,[4] may be contrasted with the dioxygen activation by the diferrous sites of methane monooxygenase (MMO),[3] ribonucleotide reductase (RR),[5] and fatty acid desaturases.[6]

Binding of O_2 to Hr is a reversible process in which two electrons from the diferrous active site are transferred to O_2 to form a binuclear Fe(III) complex with a terminal hydroperoxide.[4] The reduction of dioxygen to the peroxide level is confirmed by the appearance of a new intense absorption band at ∼500 nm in the optical spectrum of oxyHr, assigned to a hydroperoxide-to-Fe charge transfer (CT) transition on the basis of resonance Raman data[7] and polarized single-crystal absorption spectra.[8] In contrast to Hr, reduced MMO reacts with O_2 in an irreversible process forming a peroxide intermediate (designated P[9]) that was trapped and studied spectroscopically.[10] The Mössbauer data show that both ions are ferric and suggest that peroxide binds in a symmetric end-on μ-1,2 or side-on μ-η^2:η^2 mode. The optical absorption spectrum exhibits an intense band centered at ∼625 nm (ϵ = 1500 M^{-1} cm^{-1}), assigned to a peroxide-to-Fe CT transition by reference to a similar feature

[†] Stanford University.
[‡] Tokyo Institute of Technology.

(1) Babcock, G. T.; Floris, R.; Nilsson, T.; Pressler, M.; Varotsis, C.; Vollenbrock, E. *Inorg. Chim. Acta* **1996**, *243*, 345.
(2) Feig, A. L.; Lippard, S. J. *Chem. Rev.* **1994**, *94*, 759.
(3) Wallar, B. J.; Lipscomb, J. D. *Chem. Rev.* **1996**, *96*, 2625.
(4) Stenkamp, R. E. *Chem. Rev.* **1994**, *94*, 715.
(5) Logan, D. T.; Su, X.-D.; Åberg, A.; Regnström, K.; Hajdu, J.; Eklund, H.; Nordlund, P. *Struct. Bonding (Berlin)* **1996**, *4*, 1053.
(6) Lindqvist, Y.; Huang, W.; Schneider, G.; Shanklin, J. *EMBO J.* **1996**, *15*, 4081.
(7) Shiemke, A. K.; Loehr, T. M.; Sanders-Loehr, J. *J. Am. Chem. Soc.* **1986**, *108*, 2437.
(8) Gay, R. R.; Solomon, E. I. *J. Am. Chem. Soc.* **1978**, *100*, 1972.
(9) This species has also been termed L or H_{peroxo} in the literature.[3,10]
(10) (a) Liu, K. E.; Wang, D.; Huynh, B. H.; Edmondson, D. E.; Salifoglou, A.; Lippard, S. J. *J. Am. Chem. Soc.* **1994**, *116*, 7465. (b) Liu, K. E.; Valentine, A. M.; Qiu, D.; Edmondson, D. E.; Appelman, E. H.; Spiro, T. G.; Lippard, S. J. *J. Am. Chem. Soc.* **1995**, *117*, 4997 and corrections *J. Am. Chem. Soc.* **1997**, *119*, 11134.

S0002-7863(98)00129-2 CCC: $15.00
Published on Web 05/28/1998

in the spectra of Fe(III)−peroxide model complexes.[10] There are also preliminary Mössbauer data suggesting that a peroxide intermediate similar to *P* occurs by the reaction of the reduced RR with O_2,[11] supporting recent proposals of a common mechanism for dioxygen activation by MMO and RR.[2,12,13]

Studies of binuclear iron model complexes have contributed much to the current understanding of the spectroscopic and catalytic properties of the active sites in non-heme iron proteins.[3] Much effort has been undertaken to design synthetic non-heme iron(II) complexes that can bind O_2 as peroxide and thus mimic the reactions of MMO and RR with dioxygen. Many proposed μ-1,2 peroxide-bridged Fe(III) dimers have been characterized in solution, and they all exhibit an intense absorption band at ∼600 nm and an unusually high O−O stretching frequency of 850−900 cm^{-1}.[3] Recently these efforts culminated in the first crystal structures of binuclear Fe(III)−peroxide complexes. In the three structurally characterized complexes known to date,[14−16] peroxide coordinates to the two Fe(III) atoms in a cis μ-1,2 bridging mode, with Fe−O−O−Fe dihedral angles varying from 0 to 53°. The O−O bond lengths are ∼1.42 Å, characteristic of peroxide, and the average Fe−O bond length of 1.88 Å is comparable with terminal Fe(III)−OH bond lengths. Interestingly, the Fe−O−O angles of 120−129° are significantly larger than the metal−O−O angles found in μ-1,2 peroxide-bridged Cu(II) and Co(III) dimers (∼110°).[17,18] All three complexes exhibit an optical absorption spectrum similar to the one reported for MMO intermediate *P*, and the Mössbauer parameters for one of the complexes, [Fe$_2$(O$_2$)(O$_2$CCH$_2$C$_6$H$_5$)$_2${HB(pz′)$_3$}$_2$],[16] and *P*[10] are practically identical and very unusual for carboxylate-bridged Fe(III) dimers. Therefore, a cis μ-1,2 peroxide diiron(III) core structure is currently favored for the peroxide intermediate *P*.[3,12,19] This proposal is supported by recent theoretical studies that addressed the nature of the intermediates in the MMO reaction cycle. Both extended Hückel[20] and density functional calculations[21,22] suggest that a cis μ-1,2 bridging mode is the most favorable binding mode of peroxide to the active site of MMO. In one case, the model used had a low coordination number of 4 for each Fe atom which would favor further peroxide coordination, and a lowest-energy structure for *P* was obtained with one Fe atom exhibiting η^2 coordination to peroxide.[21]

In the following we report a detailed vibrational and optical spectroscopic study of the cis μ-1,2 peroxide-bridged diiron(III) complex [Fe$_2$(O$_2$)(OBz)$_2${HB(pz′)$_3$}$_2$] (see Chart 1 for a schematic illustration of the dimer core structure). A normal coordinate analysis (NCA) is presented that addresses the origin of the unusually high O−O stretching frequency generally observed in cis μ-1,2 peroxide-bridged Fe(III) dimers. A complete assignment of the peroxide-to-Fe CT absorption spectrum is given and used to separate the π and σ contributions to the Fe−peroxide bonding interaction. To obtain further insight into the electronic structure of cis μ-1,2 peroxide-bridged Fe(III) dimers, the experimental data are complemented by density functional calculations. A description of Fe−peroxide bonding is developed and compared with Cu−peroxide bonding in a series of well-characterized Cu(II)−peroxide models. The source of the large metal−O−O bond angles in Fe(III)−peroxide dimers is discussed in the light of the unique iron−peroxide bonding interaction involving a significant π contribution. The negative charge on peroxide in [Fe$_2$(O$_2$)(OBz)$_2$-{HB(pz′)$_3$}$_2$] is evaluated relative to the series of Cu−peroxide complexes, and the mechanistic implications for the conversion of the putative cis μ-1,2 peroxide-bridged intermediate *P* to a high-valent diiron(IV)−oxo species are discussed. Finally, differences in the effectiveness of peroxide and oxo bridges in mediating antiferromagnetic coupling in Fe(III) dimers are explored.

Chart 1. Core Atoms of [Fe$_2$(O$_2$)(OBz)$_2${HB(pz′)$_3$}$_2$] and Coordinate Frames

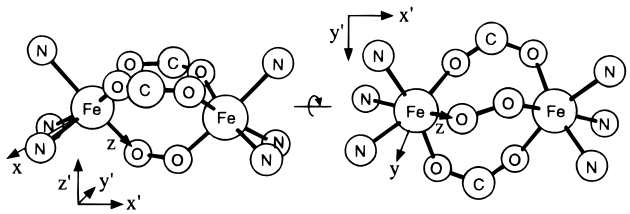

Experimental Section

A microcrystalline precipitate of the blue-green dioxygen complex [Fe$_2$(O$_2$)(OBz)$_2${HB(pz′)$_3$}$_2$], where HB(pz′)$_3$ = hydrotris(3,5-diisopropyl-1-pyrazolyl)borate and OBz = benzoate, was obtained from the reaction of the ferrous precursor [Fe{HB(pz′)$_3$}(OBz)] with dioxygen in a pentane solution at −78 °C, according to Kitajima et al.[23] The complex is thermally unstable and was maintained below −70 °C. For the preparation of $^{18}O_2$-substituted samples used for Raman experiments, the solid was dissolved in toluene at −20 °C, and the resulting solution was deoxygenated by purging with N_2 gas, reoxygenated with $^{18}O_2$, and slowly frozen in liquid N_2.

Variable temperature absorption spectra were measured on a double-beam spectrophotometer (Cary 17) using a liquid helium cryostat (Janis Research Super Vari-Temp). Magnetic circular dichroism (MCD) data were collected on CD spectropolarimeters (JASCO J500, S1 and S20 PM tubes for UV/vis/near-IR regions, and JASCO J200, InSb detector for near-IR region) with sample compartments modified to accommodate magnetocryostats (Oxford Instruments, SM4-7T). Mulls were prepared in a glovebag purged with nitrogen gas by grinding the solid material in a mortar embedded in dry ice. The fine powder was suspended in Nujol mulling agent and spread between precooled quartz disks. For the preparation of toluene solution and glass samples, cold solvent (∼−50 °C) was injected into a precooled sample cell containing small amounts of solid material finely divided between two quartz disks that were separated by a Viton O-ring spacer.

Raman spectra were obtained using a series of lines of Kr^+ (Coherent I90C−K) and Ar^+ (Coherent Sabre 25/7) ion lasers with incident power in the 5−25 mW range using an ∼135° backscattering arrangement. The scattered light was dispersed by a triple monochromator (Spex 1877 CP, equipped with 1200, 1800, and 2400 grooves/mm gratings)

(11) Tong, W. H.; Chen, S.; Lloyd, S. G.; Edmondson, D. E.; Huynh, B. H.; Stubbe, J. *J. Am. Chem. Soc.* **1996**, *118*, 2107.
(12) (a) Que, L., Jr.; Dong, Y. *Acc. Chem. Res.* **1996**, *29*, 190. (b) Que, L., Jr. *J. Chem. Soc., Dalton Trans.* **1997**, 3933.
(13) Edmondson, D. E.; Huynh, B. H. *Inorg. Chim. Acta* **1996**, *252*, 399.
(14) Ookubo, T.; Sugimoto, H.; Nagayama, T.; Masuda, H.; Sato, T.; Tanaka, K.; Maeda, Y.; Okawa, H.; Hayashi, Y.; Uehara, A.; Suzuki, M. *J. Am. Chem. Soc.* **1996**, *118*, 701.
(15) Dong, Y.; Yan, S.; Young, V. G., Jr.; Que, L., Jr. *Angew. Chem., Int. Ed. Engl.* **1996**, *35*, 618.
(16) Kim, K.; Lippard, S. J. *J. Am. Chem. Soc.* **1996**, *118*, 4914.
(17) Jacobson, R. R.; Tyeklár, Z.; Farooq, A.; Karlin, K. D.; Liu, S.; Zubieta, J. *J. Am. Chem. Soc.* **1988**, *110*, 3690.
(18) Niederhoffer, E. C.; Timmons, J. H.; Martell, A. E. *Chem. Rev.* **1984**, *84*, 137.
(19) Valentine, A. M.; Lippard, S. J. *J. Chem. Soc., Dalton Trans.* **1997**, 3925.
(20) (a) Yoshizawa, K.; Hoffmann, R. *Inorg. Chem.* **1996**, *35*, 2409. (b) Yoshizawa, K.; Yamabe, T.; Hoffmann, R. *New J. Chem.* **1997**, *21*, 151.
(21) Siegbahn, P. E. M.; Crabtree, R. H. *J. Am. Chem. Soc.* **1997**, *119*, 3103.
(22) Yoshizawa, K.; Yokomichi, Y.; Shiota, Y.; Ohta, T.; Yamabe, T. *Chem. Lett.* **1997**, 587.
(23) Kitajima, N.; Tamura, N.; Amagai, H.; Fukui, H.; Moro-oka, Y.; Mizutani, Y.; Kitagawa, T.; Mathur, R.; Heerwegh, K.; Reed, C. A.; Randall, C. R.; Que, L., Jr.; Tatsumi, K. *J. Am. Chem. Soc.* **1994**, *116*, 9071.

and detected with a back-illuminated CCD camera (Princeton Instruments ST-135). Attempts to obtain a resonance Raman spectrum from solid and solution samples spun in sealed quartz capillary or electron paramagnetic resonance (EPR) tubes and cooled to ∼170 K using a nitrogen gas flow system were unsuccessful because of rapid photodecomposition of $[Fe_2(O_2)(OBz)_2\{HB(pz')_3\}_2]$. The decomposition rate could be greatly reduced by freezing the sample, and the Raman spectra presented here were measured in a toluene glass at 77 K using an EPR dewar filled with liquid N_2. Profiles were obtained by measuring the Raman spectra of at least five samples, first with excitation at 799 nm to scale the intensities, then at the wavelength of interest, and subsequently again at 799 nm to monitor sample integrity. Background spectra of pure toluene were measured under the same conditions and were used to correct the Raman intensities for reabsorption of the scattered light by the sample. Peak intensities were determined relative to the ∼620 cm^{-1} band of the toluene solvent.[24]

A normal coordinate analysis (NCA) was performed on a C_2 idealized geometry of the $Fe_2(O_2)$ unit in the crystal structure of $[Fe_2(O_2)(O_2CCH_2C_6H_5)_2\{HB(pz')_3\}_2]$:[16,25] Fe−O = 1.885 Å, O−O = 1.408 Å, Fe−O−O angle $\gamma = 129.1°$, and Fe−O−O−Fe dihedral angle $\tau = 52.9°$. The analysis was based on a Wilson FG matrix method using a Urey−Bradley force field as implemented in a modified version of the Schachtschneider program.[26]

Density functional calculations were performed on an IBM 3BT-RS/6000 computer using the Amsterdam Density Functional (ADF) program version 2.0.1 developed by Baerends et al.[27] The structure of $[Fe_2(O_2)(OBz)_2\{HB(pz')_3\}_2]$ was approximated by a model of idealized C_2 symmetry with formates replacing the benzoates and NH_3 ligands replacing the $HB(pz')_3$ ligation. Two different views of this $[Fe_2(O_2)(O_2CH)_2(NH_3)_6]^{2+}$ model together with the molecular (primed) and local (unprimed) coordinate frames used throughout this study are shown in Chart 1. The $Fe_2(O_2)$ core is identical to the one used for the NCA. Note that compared with the commonly used axes orientation, the **x** and **y** axes are rotated around **z** by 45°; thus, the e_g set of Fe d orbitals comprises the z^2 and xy orbitals. Complete coordinates of all the models used for the calculations presented in the text are included in the Supporting Information.

A triple-ζ Slater-type orbital basis set (ADF basis set IV) with a single polarization function was used for each atom. Core orbitals were frozen through 1s (C, N, O) and 3p (Fe). All calculations were performed using the local density approximation of Vosko, Wilk, and Nusair[28] for the exchange and correlation energy and the nonlocal gradient corrections of Becke[29] and Perdew.[30] Geometries were optimized by using the algorithm of Versluis and Ziegler[31] provided in the ADF package and were considered converged when the changes in bond lengths between subsequent iterations fell below 0.01 Å. Graphical output of the computational results was generated with the Cerius[2] software program developed by Molecular Simulations Inc.

Results

Spectroscopic. Figure 1 shows the solid-state mull absorption spectra of $[Fe_2(O_2)(OBz)_2\{HB(pz')_3\}_2]$ at 15 and 200 K. At 15 K, an intense broad band with a maximum at 14600 cm^{-1} (ϵ = 3850 M^{-1} cm^{-1}) extends from ∼10 000 to 19 000 cm^{-1}, giving rise to the blue-green color of the complex. In the UV region, two stronger bands of comparable intensity peak at 27 000 cm^{-1} (5900 M^{-1} cm^{-1}) and 33 000 cm^{-1} (6300 M^{-1} cm^{-1}), respectively, and the onset to a very intense absorption is observed above 35 000 cm^{-1}. In the spectrum obtained at 200 K, the bands are slightly broader, but their peak positions and integrated intensities are practically the same as at 15 K. The temperature dependence of the absorption spectra in Figure 1 provides important information about excited-state exchange interactions between the two Fe atoms in the dimer. From a Boltzmann analysis with a ground-state exchange-coupling constant of $J = -33$ cm^{-1} ($H = -2J\mathbf{S}_1\mathbf{S}_2$) reported for solid $[Fe_2(O_2)(OBz)_2\{HB(pz')_3\}_2]$,[23] the relative population of the $S = 0$ component of the ground state decreases from 99% at 15 K to 22% at 200 K. The intensities of the singlet−singlet transitions are thus expected to decrease by ∼80% between 15 and 200 K, accompanied by an increase in intensity of the triplet−triplet (1→41%) and quintet−quintet (0→22%) transitions. Hence, the weak temperature dependence of the three bands in Figure 1 allows us to exclude large antiferromagnetic energy splittings in the observed excited states.[32]

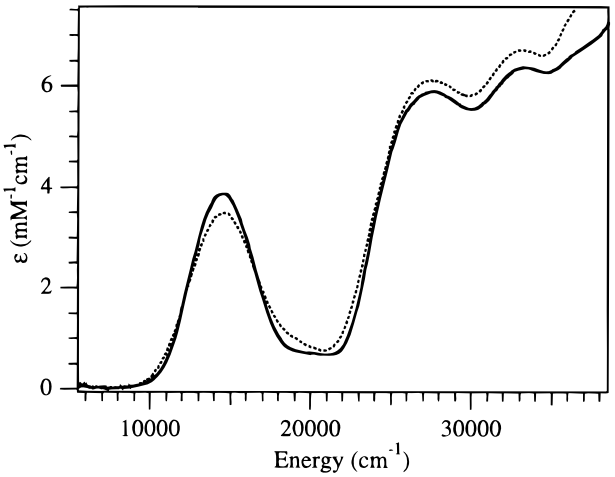

Figure 1. Solid-state mull absorption spectra of $[Fe_2(O_2)(OBz)_2\{HB(pz')_3\}_2]$ at 15 K (solid line) and 200 K (dotted line).

The resonance Raman spectrum in a toluene glass at 77 K obtained with excitation at 647 nm (15 454 cm^{-1}) is dominated by two bands at 421 and 876 cm^{-1}, respectively, shown in the insets of Figure 2. In samples prepared with $^{18}O_2$, these features shift to 409 and 828 cm^{-1} (broken lines). Similar results were previously obtained in toluene solution and led to the assignment of the two bands to the symmetric ν(Fe−O) and ν(O−O) stretching modes, respectively, of the $Fe_2(O_2)$ core.[23] In the spectrum of the $^{16}O_2$ derivative, an additional weak band peaks at 832 cm^{-1}, which we assign to the first overtone of ν(Fe−O) (vide infra). The fundamental-to-overtone ratio is ∼4/1 and constant for different excitation wavelengths in the visible region where the overtone carries sufficient intensity to be observed. Note that in the $^{18}O_2$ derivative, the corresponding feature is expected at ∼815 cm^{-1} and is thus obscured by the broad intense ν(O−O) band peaking at 828 cm^{-1}.

In Figure 2, the resonance Raman excitation profiles for the symmetric ν(Fe−O) and ν(O−O) fundamental bands in a toluene glass at 77 K are superimposed on the corresponding absorption spectrum. Both features are greatly enhanced under the visible absorption band and much less under the lower energy UV band. There is no discernible intensity enhancement in the origin region of the second UV band. The ν(Fe−O)/

(24) We found that toluene and CCl_4 exhibit the same Raman scattering behavior below 28 500 cm^{-1}.

(25) In view of the moderate resolution of the crystal structure (R = 0.142[16]), we assume that the C_2 idealized $Fe_2(O_2)$ unit derived from $[Fe_2(O_2)(O_2CCH_2C_6H_5)_2\{HB(pz')_3\}_2]$ is similarly appropriate for NCAs of the benzoate and phenylacetate derivatives.

(26) (a) Schachtschneider, J. H. Technical Report No. 57-65, Shell Development Company, Emeryville, CA, 1966. (b) Fuhrer, H.; Kartha, V. B.; Kidd, K. G.; Krueger, P. J.; Mantsch, H. H. Computer Programs for Infrared Spectroscopy, Bulletin No. 15, National Research Council of Canada, 1976.

(27) (a) Baerends, E. J.; Ellis, D. E.; Ros, P. *Chem. Phys.* **1973**, *2*, 42. (b) te Velde, G.; Baerends, E. J. *Int. J. Comput. Phys.* **1992**, *99*, 84.

(28) Vosko, S. H.; Wilk, L.; Nusair, M. *Can. J. Phys.* **1980**, *58*, 1200.

(29) Becke, A. D. *J. Chem. Phys.* **1986**, *84*, 4524.

(30) Perdew, J. P. *Phys. Rev. B* **1986**, *33*, 8822.

(31) Versluis, L.; Ziegler, T. *J. Chem. Phys.* **1988**, *88*, 322.

(32) Brown, C. A.; Remar, G. J.; Musselman, R. L.; Solomon, E. I. *Inorg. Chem.* **1995**, *34*, 688.

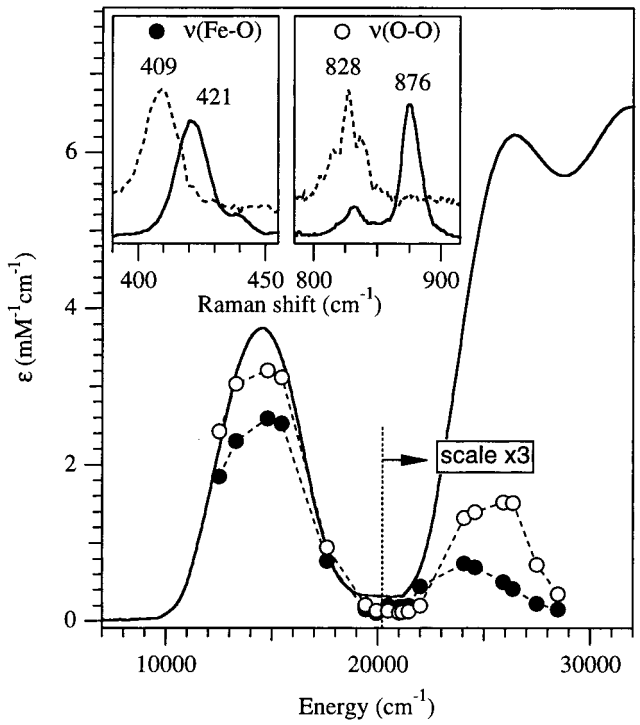

Figure 2. 77 K absorption spectrum and resonance Raman excitation profiles for the ν(Fe−O) (●) and ν(O−O) (○) fundamental bands of $[Fe_2(O_2)(OBz)_2\{HB(pz')_3\}_2]$ in a toluene glass. Note the scale change for the Raman profiles above 20 000 cm^{-1}. Insets: resonance Raman spectra of the ν(Fe−O) and ν(O−O) fundamental bands for 647 nm (15 454 cm^{-1}) excitation: solid and broken lines for $^{16}O_2$ and $^{18}O_2$ derivatives, respectively.

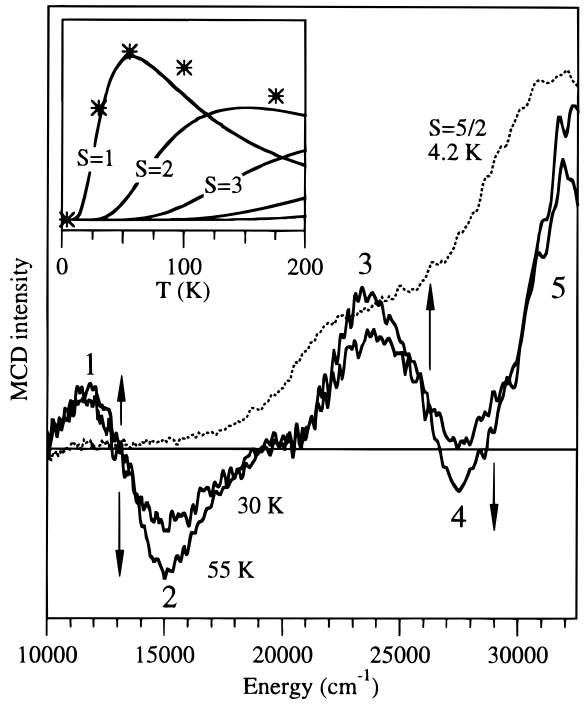

Figure 3. MCD spectra of $[Fe_2(O_2)(OBz)_2\{HB(pz')_3\}_2]$ in a mull at 4.2 K (dotted line), and 30 and 55 K (solid lines). The 30 and 55 K spectra were corrected for an $S = 5/2$ paramagnetic impurity that dominates the 4.2 K spectrum. Inset: calculated temperature dependence of the MCD intensities for transitions from each spin sublevel of the ground state (solid lines) and sum of experimental band intensities of bands 1 and 2 (*).

ν(O−O) intensity ratio is essentially constant in the visible spectral region (∼1/1.3), but exhibits a strong wavelength dependence under the lower energy UV band. The ratio reaches a maximum of ∼2/1 at 22 500 cm^{-1} and gradually decreases to ∼1/3 at 27 000 cm^{-1}, demonstrating that this band is actually composed of at least two components.

A representative 4.2 K MCD spectrum of $[Fe_2(O_2)(OBz)_2\{HB(pz')_3\}_2]$ in a mull is shown in Figure 3 (dotted line). This spectrum is practically identical in general appearance and field dependence to the spectrum of the thermal decomposition product of $[Fe_2(O_2)(OBz)_2\{HB(pz')_3\}_2]$ (not shown), and it is therefore assigned to traces of this species. With increasing temperature, however, the spectra of $[Fe_2(O_2)(OBz)_2\{HB(pz')_3\}_2]$ samples and those of the thermal decomposition product become strikingly different. Normalized variable-temperature variable-field MCD band intensities of the decomposition product are well fit by the Brillouin function for an isolated $S = 5/2$ ground state.[33] This result is consistent with a high-spin Fe(III) monomer or the crystallographically characterized, strongly antiferromagnetically coupled ($S_{tot} = 5/2$) trinuclear ferric complex that is formed in low yield from $[Fe_2(O_2)(OBz)_2\{HB(pz')_3\}_2]$ at higher temperatures.[23]

In the spectra of $[Fe_2(O_2)(OBz)_2\{HB(pz')_3\}_2]$, new bands start growing in at temperatures >∼20 K. The shapes of these bands can be estimated by subtracting the 4.2 K spectrum scaled according to the $S = 5/2$ Brillouin function to eliminate contributions from the decomposition product. The results are shown in Figure 3 for 30 and 55 K (solid lines). In this approach, the 4.2 K spectrum becomes a straight line at zero intensity, and the features observed at higher temperatures arise from species other than the primary decomposition product. The 30 and 55 K spectra consist of two pairs of bands of similar magnitude but opposite sign centered at 13 000 cm^{-1} (bands 1 and 2) and 25 000 cm^{-1} (bands 3 and 4), and a stronger band (5) with a positive maximum above 32 000 cm^{-1}, all of which increase in intensity between 30 and 55 K. The spectra obtained at higher temperatures (not shown) closely resemble the 55 K spectrum.

In exchange-coupled dimers, the temperature dependence of the *C*-term MCD intensity of transitions originating from each spin sublevel of the ground state is approximately given by the product of the respective Boltzmann population and Brillouin curve. The corresponding curves for $[Fe_2(O_2)(OBz)_2\{HB(pz')_3\}_2]$, calculated with $J = -33$ cm^{-1},[23] along with the sum of intensities of bands 1 and 2 (asterisks), are shown in the inset of Figure 3. The experimental intensities closely match the curve calculated for transitions originating from the triplet ($S = 1$) state with deviations above 55 K. These deviations are due to transitions from the $S = 2$ and $S = 3$ spin states of the ground state contributing to the observed MCD intensity at higher temperatures. Thus, on the basis of their temperature dependence, bands 1−5 are assigned to $[Fe_2(O_2)(OBz)_2\{HB(pz')_3\}_2]$. The lack of isosbestic points at zero intensity above 25 000 cm^{-1} indicates that the paramagnetic impurity is not completely compensated for in the UV range. In the lower energy, near-IR region (not shown), no MCD bands attributable to $[Fe_2(O_2)(OBz)_2\{HB(pz')_3\}_2]$ were observed.

The MCD spectra of $[Fe_2(O_2)(OBz)_2\{HB(pz')_3\}_2]$ in a toluene glass suffer from a much poorer baseline than the mull data. However, spectra of good quality were obtained in liquid toluene solution at 180 K (Figure 4, lower trace). At this temperature, the contribution from the decomposition product with an $S = 5/2$ ground state is negligible, and the fact that the solution

(33) Kittel, C. *Introduction to Solid State Physics;* 6th ed.; Wiley & Sons: New York, 1986; pp 400−402.

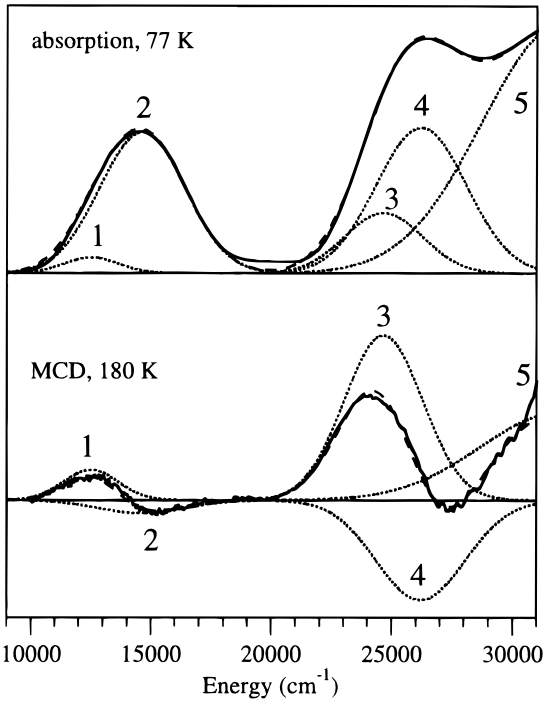

Figure 4. 77 K glass absorption spectrum (top) and 180 K solution MCD spectrum (bottom) of $[Fe_2(O_2)(OBz)_2\{HB(pz')_3\}_2]$ (solid lines). The Gaussian resolved bands obtained from a simultaneous fit of the absorption and MCD spectra and their sums are shown by the dotted and broken lines, respectively.

Table 1. Fit Parameters from Simultaneous Gaussian Resolutions of the Absorption and Correpsonding MCD Spectra in a Mull (55 K) and a Toluene Glass (Absorption, 77 K) and Solution (MCD, 180 K)[a]

sample	band	ν_{max}	$\nu_{1/2}$	ϵ_{max}	I (MCD)	$10^3 f$
mull	1	12 450	2500	300	1200	3
	2	14 630	4500	3780	−1415	78
	3	24 400	3850	2200	2130	39
	4	27 250	4600	4370	−1650	92
	5	33 150	7580	6475	3400	226
toluene	1	12 500	2660	420	800	5
	2	14 620	4180	3730	−350	72
	3	24 650	3830	1600	4430	29
	4	26 200	4400	3850	−2650	78
	5	32 000	7740	6600	2400	235

[a] Band maxima ν_{max} and bandwidths at half-maximum $\nu_{1/2}$ in cm^{-1}, molar extinction coefficients ϵ_{max} in M^{-1} cm^{-1}, MCD intensities I(MCD) in arbitrary units (different scales for mull and toluene data), and oscillator strengths f.

spectrum is similar in general appearance to the 55 K mull spectrum in Figure 3 supports our approach to resolve the MCD bands of $[Fe_2(O_2)(OBz)_2\{HB(pz')_3\}_2]$ in the solid-state spectra. In both cases, good simultaneous fits of the MCD and absorption spectra are obtained with a set of five Gaussian bands. This is shown in Figure 4 for the toluene spectra and provided as Supporting Information for the mull data (Figure S1). The high resemblance of the two sets of fit parameters (Table 1) indicates that the structure of $[Fe_2(O_2)(OBz)_2\{HB(pz')_3\}_2]$ in the solid state is maintained in solution. From the similarity of the solution absorption and Raman data of this complex and the crystallographically characterized phenylacetate derivative[16] we conclude that $[Fe_2(O_2)(OBz)_2\{HB(pz')_3\}_2]$ has an analogous cis μ-1,2 peroxide di-μ-1,3 carboxylato tribridged structure.

Computational. To further elucidate the electronic structure of binuclear cis μ-1,2 peroxide-bridged binuclear Fe(III) complexes the experimental data are complemented by full symmetry, high spin (HS), and broken symmetry (BS) spin unrestricted density functional calculations. The HS or ferromagnetic state with $S_{tot} = 5$, $|M_S| = 5$ is the only pure spin state in Fe(III) dimers that can be described by a single determinant. The relevant part of the energy level diagram obtained from a spin unrestricted HS calculation for $[Fe_2(O_2)(O_2CH)_2(NH_3)_6]^{2+}$ (Chart 1) is shown in Figure 5. The orbitals are grouped according to their transformation behavior with respect to the C_2 axis of the complex: symmetric, a (+), and antisymmetric, b (−). The 10 Fe d-based MOs arise from (+) and (−) combinations of the five monomeric d orbitals with equal single-site contributions and additional ligand contributions of the appropriate symmetry. In the ferromagnetic ground state, the five d electrons on each Fe atom fill the 10 spin-up orbitals, leading to a large stabilization of these orbitals by spin polarization relative to their unoccupied spin-down counterparts. The splitting is large enough to displace the spin-up orbitals below the occupied peroxide π^* orbitals (Figure 5, left-hand side). As a result, the Fe d-based spin-up MOs are delocalized onto the neighboring ligands and spread over a large energy range. A good description of the metal d-based MOs is obtained from the 10 lowest energy unoccupied spin-down orbitals that reflect the primarily Fe-centered excess (i.e., uncompensated) spin-up density. Energies and compositions of these orbitals and the peroxide π^*-based occupied spin-down MOs are given in Table 2.

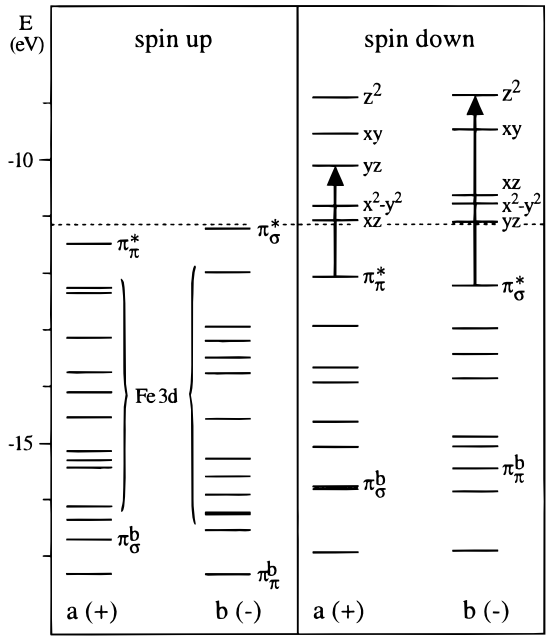

Figure 5. Energy level diagram obtained from a HS calculation on $[Fe_2(O_2)(O_2CH)_2(NH_3)_6]^{2+}$ (Chart 1). The orbitals are grouped according to their transformation behavior with respect to the C_2 axis of the complex: symmetric, a (+); and antisymmetric, b (−). The peroxide-to-Fe CT transitions corresponding to bands 2 and 4 in Figure 4 are indicated by arrows.

In the BS approach developed by Noodleman,[34] all the symmetry elements connecting the two metal ions in a dimer are removed, permitting the spin-up and spin-down densities to localize on opposite sides of the molecule. This approach introduces valence-bond concepts into density functional calculations and allows dimers to be treated as two weakly interacting antiferromagnetically coupled monomers. Although the BS single determinantal wave functions are not proper dimer functions, they provide an intuitive picture of electron delocal-

(34) Noodleman, L.; Norman, J. G., Jr. *J. Chem. Phys.* **1979**, *70*, 4903.

Table 2. Energies (eV) and Compositions (%) of the Relevant Spin-Down Molecular Orbitals from a HS Calculation on $[Fe_2(O_2)(O_2CH)_2(NH_3)_6]^{2+}$ [a]

			Fe					O(peroxide)				
level		energy	x^2-y^2	xz	yz	xy	z^2	x'	y'	z'	orb[b]	N,O′ tot[c]
						Unoccupied						
z^2 (−)	29b	−8.850	0	3	0	5	53	2	1	23	π_σ^*	10
z^2 (+)	30a	−8.898	1	1	1	5	58	4	5	2	σ^b, π_π^*	15
xy (−)	28b	−9.454	0	0	1	64	4	0	0	3		21
xy (+)	29a	−9.538	0	0	3	67	6	0	0	0		15
yz (+)	28a	−10.104	0	5	42	3	4	2	39	1	π_π^*	3
xz (−)	27b	−10.615	36	34	7	0	3	0	3	5		8
x^2-y^2 (−)	26b	−10.757	48	24	7	0	3	0	2	5		9
xz (+)	27a	−10.808	13	67	9	1	2	0	0	3		2
x^2-y^2 (+)	26a	−11.061	78	11	2	0	0	0	0	1		2
yz (−)	25b	−11.080	0	11	76	1	1	3	1	1		2
						Occupied						
π_π^*	25a	−12.054	0	7	33	1	1	3	40	0		12
π_σ^*	24b	−12.206	0	17	0	0	11	0	0	51		17

[a] Fe d and O(peroxide) p orbitals are labeled using an abbreviated notation; e.g., *xz* stands for d_{xz} (see Chart 1 for axes orientations). [b] Nature of peroxide orbital interacting with the corresponding Fe d-based orbital. [c] Total contributions from $N(NH_3)$ and O′(formate).

Table 3. Energies (eV) and Compositions (%) of the Unoccupied Spin-Down Orbitals Localized on Fe1, Obtained from a BS Calculation on $[Fe_2(O_2)(O_2CH)_2(NH_3)_6]^{2+}$ [a]

		left		peroxide			right	
level	energy	N,O′	Fe1	O1	O2	orb	Fe2	N,O′
z^2	−8.921	11	67	8	4	π_σ^*	0	0
xy	−9.373	16	73	1	1		0	1
yz	−10.393	0	61	22	10	π_π^*	3 z^2	0
x^2-y^2	−10.672	6	83	3	2		0	2
xz	−10.861	2	79	5	4	π_σ^*	3 z^2	3

[a] Fe d, O1,O2(peroxide) p, and total $N(NH_3)$, O′(formate) orbital contributions.

ization in exchange-coupled systems. Energies and compositions of the Fe1 d-based unoccupied spin-down orbitals obtained from a spin unrestricted BS calculation on $[Fe_2(O_2)(O_2CH)_2(NH_3)_6]^{2+}$ in C_1 symmetry are given in Table 3, and an energy level diagram is shown in Figure S2 (Supporting Information).

The BS state, represented by a single Slater determinant, is a weighted average of the $M_S = 0$ components of the pure spin states $S_{tot} = 0, 1, ..., 5$. Using the formalism developed by Noodleman,[35] the ground-state exchange-coupling constant J can be calculated from the energies, E, of the HS ($S_{tot} = S_{max} = 5$) and BS states:

$$J = -(E_{HS} - E_{BS})/{S_{max}}^2 \quad (1)$$

With the calculated total energies of the HS and BS states, a value of $J = -128$ cm^{-1} is obtained, which is roughly a factor of 4 larger than the experimental value.[23] The overestimation of exchange-coupling constants by a factor of 2−4 is typical of density functional calculations,[32,36,37] and the significance of this result is that the calculation predicts the correct sign for J; that is, that the two Fe atoms are weakly antiferromagnetically coupled.

Analysis

Normal-Coordinate Analysis. A striking feature of cis μ-1,2 peroxide-bridged diiron(III) complexes is their high O−O stretching frequency, typically observed in the range 850−900 cm^{-1}.[3] In most cases, the shifts occurring upon $^{16}O_2 \rightarrow {}^{18}O_2$ isotopic substitution are in good agreement with the shifts calculated for an isolated O−O oscillator. This result would appear to indicate that mechanical coupling can be excluded as a source of the high O−O stretching frequency, implying that the O−O force constant is high. To correlate the high O−O stretching frequency to the bond strength, we performed a NCA of the $Fe_2(O_2)$ unit in $[Fe_2(O_2)(OBz)_2\{HB(pz')_3\}_2]$ using the Raman data presented in Figure 2 and the structural parameters of the phenylacetate analog.[16,25] A Urey−Bradly force field was chosen to facilitate comparison with the results from NCAs performed on Cu−peroxide complexes using this type of force field.[38]

The $Fe_2(O_2)$ unit has 6 vibrational degrees of freedom. To reduce the number of parameters, the torsional mode was not included at the first stage of the analysis, leaving three symmetry inequivalent internal coordinates: the Fe−O and O−O stretching coordinates and the Fe−O−O bending coordinate. The corresponding force constants, together with an Fe···O nonbonded interaction constant required by the Urey−Bradly force field, were fitted for best reproduction of the experimental frequencies. The results from the fit are summarized in Table 4. For comparison, Table 4 includes the Fe−O and O−O force constants, along with the stretching frequencies for the $^{18}O_2$ derivative, calculated in the limit of isolated Fe−O and O−O harmonic oscillators. In this approximation, the force constant k (mdyn/Å) is given by

$$k = 5.892 \times 10^{-7}\, \nu^2 \mu \quad (2)$$

where ν is the vibrational frequency (cm^{-1}) and μ is the reduced mass (g/mol) of the diatomic oscillator; $\mu_{FeO} = 12.44$ g/mol and $\mu_{OO} = 8.00$ g/mol.

Table 4 shows that both calculations reproduce the experimental frequencies equally well, although the two sets of force constants are strikingly different. Similar results were obtained from an analysis of the vibrational data of the phenylacetate analogue where the O−O and Fe−O stretches occur at 888 and 415 cm^{-1}, respectively.[16] The fitted O−O force constants are 3.72 mdyn/Å (harmonic oscillator model) and 3.18 mdyn/Å (NCA) (Table S1, Supporting Information). Interestingly, the O−O force constants from the NCAs are practically identical to the one obtained from a NCA on a trans μ-1,2 peroxide-

(35) Noodleman, L. *J. Chem. Phys.* **1981**, *74*, 5737.
(36) Zhao, X. G.; Richardson, W. H.; Chen, J.-L.; Li, J.; Noodleman, L.; Tsai, H.-L.; Hendrickson, D. N. *Inorg. Chem.* **1997**, *36*, 1198.
(37) McGrady, J. E.; Stranger, R. *J. Am. Chem. Soc.* **1997**, *119*, 8512.
(38) Baldwin, M. J.; Root, D. E.; Pate, J. E.; Fujisawa, K.; Kitajima, N.; Solomon, E. I. *J. Am. Chem. Soc.* **1992**, *114*, 10421.

Table 4. Observed and Calculated Vibrational Frequencies for $[Fe_2(O_2)(OBz)_2\{HB(pz')_3\}_2]$[a]

	obsd frequencies		harmonic oscillator[b]			NCA[c]		
normal mode	$^{16}O_2$	$^{18}O_2$	$^{16}O_2$	$^{18}O_2$	force constants	$^{16}O_2$	$^{18}O_2$	force constants
ν(O−O)	876	828	876	826	$k_{O-O} = 3.62$	877	828	$k_{O-O} = 3.07$
ν_{as}(Fe−O)						550	524	
ν(Fe−O)	421	409	421	402	$k_{Fe-O} = 1.30$	423	406	$k_{Fe-O} = 1.99$
δ_{as}(Fe−O−O)						282	268	
δ(Fe−O−O)						142	136	0.31 (0.10)[d]

[a] Frequencies are in cm^{-1} and stretching force constants k in mdyn/Å. [b] Assumes isolated O−O and Fe−O harmonic oscillators. [c] From normal coordinate analysis (NCA) of the $Fe_2(O_2)$ unit. [d] Fe−O−O bending force constant (mdynÅ/rad^2), Fe···O nonbonded interaction constant (mdyn/Å) in parentheses.

Table 5. Normal Mode Descriptions for the $Fe_2(O_2)$ Unit

normal	eigenvectors[a]			PED[b]			
mode	O−O	Fe−O	Fe−O−O	O−O	Fe−O	Fe−O−O	μ_{eff}[c]
ν(O−O)	−0.35	0.14	0.05	81	18	0	6.0
ν_{as}(Fe−O)	0.00	±0.20	±0.18	0	88	11	7.1
ν(Fe−O)	0.07	0.14	0.11	13	76	7	14.4

[a] Mass-weighted eigenvectors $\mathbf{L}_n$. [b] Potential energy distribution (PED) contributions (%). [c] Effective reduced masses (g/mol), obtained from rediagonalization of the **G** matrix along the normal coordinates.

bridged Cu dimer, $k_{O-O} = 3.10$ mdyn/Å,[39] although the O−O stretching frequency is only 832 cm^{-1} in the Cu complex. Because the O−O bond strength can play an important role in determining the reactivity of metal−peroxide complexes, a series of calculations were performed to determine the sensitivity of k_{O-O} to changes in the other force constants and structural parameters, and to explore the origin of the high O−O stretching frequency in cis μ-1,2 peroxide-bridged Fe(III) dimers.

In a first set of calculations, one of the force constants was kept fixed and the rest of the force field was allowed to refine. Varying k_{Fe-O} by ±10% or the Fe−O−O bending force constant by ±50% led to changes in k_{O-O} of <0.03 mdyn/Å (Figures S3 and S4, Supporting Information). If, on the other hand, the O−O force constant was assigned a fixed value, reasonable fits to the experimental frequencies were obtained only if k_{O-O} was kept <3.30 mdyn/Å, and the quality of the fits decreased with increasing k_{O-O}.

Inclusion of the Fe−O−O−Fe torsional mode did not improve the quality of the fits or allow for values of k_{O-O} >3.30 mdyn/Å. To monitor the effect of this mode, the corresponding force constant was increased from 0 to 0.25 mdynÅ/rad^2. This led to significant mixing between the torsional mode and the Fe−O−O bending mode, but the changes in k_{O-O} were <0.08 mdyn/Å, demonstrating that the torsional mode and the O−O stretching mode are essentially uncoupled.

From these results, it is concluded that the O−O force constant is well determined by the four observed vibrational frequencies and only exhibits a weak dependence on the other force constants. Thus, the high O−O stretching frequency of 876 cm^{-1} in $[Fe_2(O_2)(OBz)_2\{HB(pz')_3\}_2]$ *does not* reflect a strong O−O bond. An explanation of this result is provided by the eigenvectors of the normal modes and the corresponding potential energy distribution (PED) contributions given in Table 5. The O−O and symmetric Fe−O stretching motions are significantly mixed because of mechanical coupling. As a consequence, the effective reduced mass μ_{eff} for ν(O−O) is lowered from 8.0 g/mol in O_2 to 6.0 g/mol in $[Fe_2(O_2)(OBz)_2\{HB(pz')_3\}_2]$ (last column in Table 5), leading to the high O−O stretching frequency.[40,41]

It is important to note that while mechanical coupling was found to be negligible in the trans μ-1,2 peroxide-bridged Cu dimer,[39] it turns out to be significant in $[Fe_2(O_2)(OBz)_2\{HB(pz')_3\}_2]$. To identify the factors that govern the mechanical coupling strength in μ-1,2 peroxide-bridged complexes, we systematically varied the structural parameters of the $Fe_2(O_2)$ unit and calculated the vibrational frequencies using the force constants of Table 4. In Figures 6A and 6B, the calculated O−O and Fe−O stretching frequencies and their respective $^{16}O_2 \rightarrow {}^{18}O_2$ isotope shifts are plotted as a function of the Fe−O−O−Fe dihedral angle τ and the Fe−O−O angle γ (for $\tau = 0°$), respectively. Upon cis → trans conversion, the Fe−O stretching frequency increases from 416 to 506 cm^{-1}, but the O−O stretching frequency is practically constant (Figure 6A, top). It is thus very unlikely that the different coupling strengths in the trans Cu dimer and $[Fe_2(O_2)(OBz)_2\{HB(pz')_3\}_2]$ arise from the structural variation along the torsional coordinate τ. In contrast, both the O−O and Fe−O stretching frequencies exhibit a strong dependence on γ (Figure 6B, top). Between $\gamma = 90°$ and 140°, the O−O stretching frequency increases from 815 to 901 cm^{-1} due strictly to mechanical coupling effects. The coupling strength is reflected in the corresponding potential energy distributions that show the O−O stretch contribution to decrease from 98 to 77% with a concomitant increase of the Fe−O stretch contribution from 0 to 22%. In the trans μ-1,2 peroxide-bridged Cu dimer, the Cu−O−O angle is only 108°,[17] as compared with $\gamma = 129°$ assumed for $[Fe_2(O_2)(OBz)_2\{HB(pz')_3\}_2]$ based on the structure of the phenylacetate analog.[16,25] We conclude that it is this difference in structure rather than O−O bond strength that causes the O−O stretching frequency to be 44 cm^{-1} higher in the Fe complex.[42,43] Interestingly, coupling between the O−O and Fe−O stretches is not apparent from the $^{16}O_2 \rightarrow {}^{18}O_2$ isotope shifts. In particular, for ν(O−O), the shifts obtained from the NCA for variations in both γ and τ barely differ from the shifts expected for an isolated O−O oscillator (Figures 6A and 6B, bottom). This is due to the fact that the Fe−O stretch contributing to ν(O−O) also primarily involves oxygen motion and thus exhibits a similar dependence on $^{16}O_2 \rightarrow {}^{18}O_2$ isotopic substitution as does the O−O stretch.

(39) Baldwin, M. J.; Ross, P. K.; Pate, J. E.; Tyeklár, Z.; Karlin, K. D.; Solomon, E. I. *J. Am. Chem. Soc.* **1991**, *113*, 8671.

(40) Note that the effective reduced mass μ_{eff} for each normal mode is determined by the **G** matrix elements that depend on the spatial arrangement of the atoms (see ref 41).

(41) Wilson, E. B., Jr.; Decius, J. C.; Cross, P. C. *Molecular Vibrations*; McGraw-Hill: New York, 1955.

(42) For comparison, the O−O force constant k_{O-O} for the crystallographically characterized complex $[Fe_2(N\text{-Et-HPTB})(Ph_3PO)_2(O_2)]^{3+}$ [15] was estimated from a NCA of the vibrational data in solution [ν(O−O) = 900 cm^{-1}] where the two Ph_3PO ligands are thought to be replaced by a bridging benzoate[43] (Table S1, Supporting Information). We obtained $k_{O-O} = 3.82$ mdyn/Å (harmonic oscillator, eq 2) and 3.26 mdyn/Å (NCA), suggesting that mixing between the Fe−O and O−O stretch motions likely contributes to the high O−O stretching frequency in this complex, similar to the case of $[Fe_2(O_2)(OBz)_2\{HB(pz')_3\}_2]$.

(43) Dong, Y.; Ménage, S.; Brennan, B. A.; Elgren, T. E.; Jang, H. G.; Pearce, L. L.; Que, L., Jr. *J. Am. Chem. Soc.* **1993**, *115*, 1851.

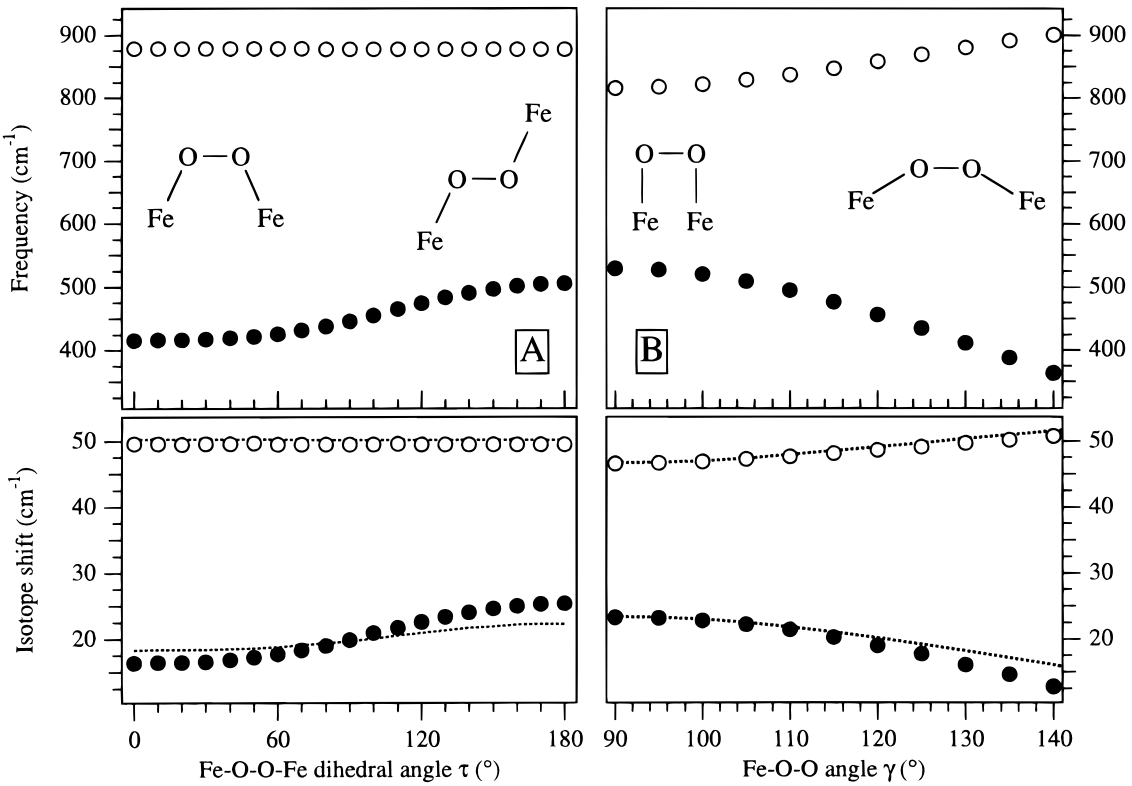

Figure 6. Calculated O−O (○) and symmetric Fe−O (●) stretching frequencies (top) and their respective $^{16}O_2 \rightarrow {}^{18}O_2$ isotope shifts (bottom) as a function of (A) the Fe−O−O−Fe dihedral angle τ and (B) the Fe−O−O angle γ (for $\tau = 0°$). The dotted lines in the lower graphs show the $^{16}O_2 \rightarrow {}^{18}O_2$ isotope shifts calculated in the limit of isolated O−O and Fe−O harmonic oscillators.

In summary, the results obtained from the normal coordinate analysis demonstrate that $^{16}O_2 \rightarrow {}^{18}O_2$ isotope shifts do not, in general, allow mechanical coupling to be excluded as a source of the high O−O stretching frequency in cis μ-1,2 peroxide-bridged binuclear complexes. The high O−O stretching frequency observed for $[Fe_2(O_2)(OBz)_2\{HB(pz')_3\}_2]$ does not reflect a strong O−O bond, but rather results from mechanical coupling between the O−O and Fe−O stretch motions. The coupling strength critically depends on the metal−O−O bond angle, and this angle is larger in the structurally characterized Fe−peroxide dimers[14−16] than in μ-1,2 peroxide-bridged Cu and Co dimers.[39,18] The origin of this structural difference will be explored in the *Discussion*.

Nature of the Fe−Peroxide Bond. One major goal of this study is to explore the nature of the Fe−peroxide bond in binuclear cis μ-1,2 peroxide-bridged Fe(III) complexes. In view of the good correspondence between the experimental and calculated J values and transition energies (vide infra), it is appropriate to use the results from the calculations on $[Fe_2(O_2)(O_2CH)_2(NH_3)_6]^{2+}$ (see *Computational* section) to identify the dominant bonding interactions between Fe and peroxide. In the following sections, the computational results will be complemented by the spectroscopic data to obtain quantitative information about Fe−peroxide bonding in $[Fe_2(O_2)(OBz)_2\{HB(pz')_3\}_2]$.

When peroxide bridges between two Fe(III) ions, the highest energy occupied peroxide π^* orbitals split into two nondegenerate levels, designated π^*_π and π^*_σ in Figure 5. The corresponding boundary surface plots (Figure 7, bottom) indicate that both π^* orbitals are involved in bonding interactions with iron. The π^*_π orbital lies in a plane perpendicular to the C_2 axis of the complex (**x′y′** plane in Chart 1) and has a strong π-bonding interaction with the symmetric (+) combination of the Fe *yz* orbitals (level 25a, Table 2). (Throughout this study we will use an abbreviated notation for p and d orbitals; e.g., *yz* standing for d_{yz}.) Note that in Cu− and Co−peroxide complexes, this corresponds to the π^*_v orbital, which is only weakly interacting with fully occupied metal d orbitals. Here, the π^*_π designation is introduced to indicate the strong π-bonding interaction with Fe. The π^*_σ orbital is oriented in the plane containing the C_2 axis and is σ bonding with the Fe *xz* and z^2 orbitals (level 24b in Table 2). The small energy splitting between the π^*_π and π^*_σ orbitals (Figure 5, Table 2) suggests that the π-bonding interaction between Fe and peroxide produces a significant contribution to the Fe−peroxide bond.

The Fe−peroxide-bonding interactions are reflected in the iron d-based unoccupied orbitals that are antibonding to peroxide. Surface plots of the relevant MOs obtained from the HS and BS calculations on $[Fe_2(O_2)(O_2CH)_2(NH_3)_6]^{2+}$ are shown in Figure 7 (top) and Figure 8, respectively. The dominant bonding interactions involve the Fe(*yz*)−peroxide(π^*_π) and Fe(z^2)−peroxide(π^*_σ) orbitals (Table 2, levels 28a and 29b, and Table 3), leading to a large destabilization of the Fe *yz*- and z^2-based MOs, consistent with peroxide being a strong-field ligand. Note that the π^*_σ orbital is more strongly stabilized than the π^*_π orbital (Figures 5 and S2) although the peroxide π^*_π character in the *yz*-based MOs is higher than the π^*_σ character in the z^2-based MOs (Tables 2 and 3). An explanation for this result is found from perturbation theory: The mixing coefficients exhibit a quadratic dependence on the energy separation, ΔE, between interacting orbitals, whereas the stabilization energy scales linearly with ΔE.

The Fe2 and peroxide π^* character in the Fe1 d-based orbitals obtained from the BS calculation (Figure 8, Table 3) reflects the effectiveness of these MOs as superexchange pathways. Hence, the "crossed" Fe1(*yz*)−peroxide(π^*_π)−Fe2(z^2) and Fe1-(*xz*)−peroxide(π^*_σ)−Fe2(z^2) pathways, involving different d orbitals on the two Fe atoms, make the dominant contribution

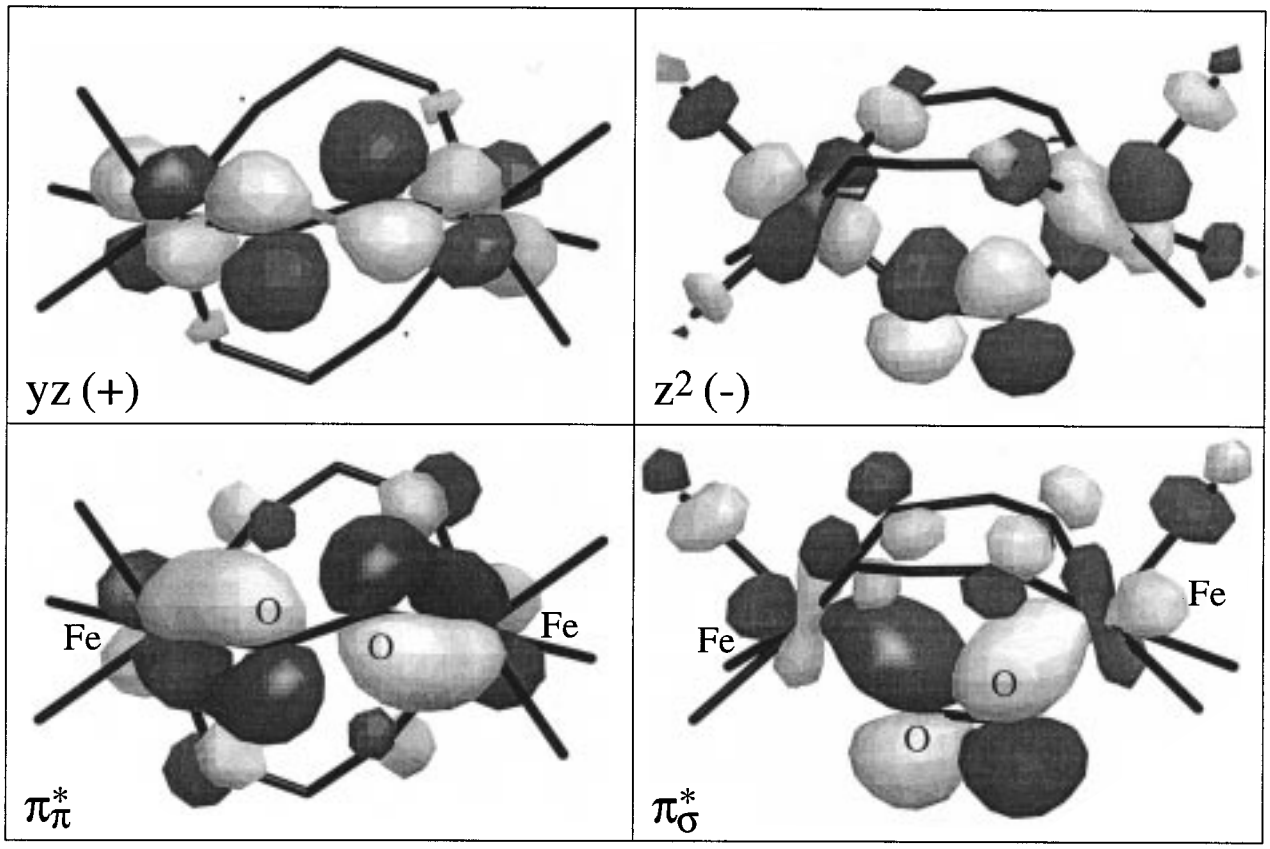

Figure 7. Surface plots of the peroxide π^*-based occupied spin-down MOs (bottom) and relevant Fe d-based unoccupied spin-down MOs (top) obtained from a HS calculation on $[Fe_2(O_2)(O_2CH)_2(NH_3)_6]^{2+}$.

to exchange-coupling in $[Fe_2(O_2)(OBz)_2\{HB(pz')_3\}_2]$. In an effort to understand the influence of the Fe−O−O and Fe−O−O−Fe angles on the exchange-coupling constant *J*, density functional calculations were performed on two additional models. The first model was constructed from $[Fe_2(O_2)(O_2CH)_2(NH_3)_6]^{2+}$ by changing the Fe−O−O−Fe dihedral angle τ from 53° to 0°, and the second model was derived from the first one by reducing the Fe−O−O angle γ from 129° to 120°. Structural changes in the Fe ligation were reduced to a minimum to facilitate comparison among the three models. Table 6 compares the relevant results for the three peroxide structures and a bent μ-oxo-bridged Fe(III) model, $[Fe_2O(O_2CH)_2(NH_3)_6]^{2+}$ (Fe−O−Fe angle of 120°), which serves as a well-defined reference complex.[44] The calculated *J* values for the three peroxide structures are similar to each other and roughly a factor of 3 smaller in magnitude than the *J* value obtained for the μ-oxo dimer [J(exp) = −120 cm^{-1} [32]]. The weak dependence of *J* on the dihedral angle τ of the peroxide models results from the interplay between the crossed Fe1(yz)−peroxide(π^*_π)−Fe2(z^2) and Fe1(xz)−peroxide(π^*_σ)−Fe2(z^2) pathways, which minimize and maximize at different angles [note that in the planar structures, the Fe1(yz)−peroxide(π^*_π)−Fe2(z^2) pathway is eliminated by symmetry]. In the planar peroxide-bridged models, the low sensitivity of *J* to changes in the Fe−O−O angle γ derives from the fact that the Fe1(xz)−peroxide(π^*_σ) interaction maximizes for γ = 180°, whereas the peroxide-(π^*_σ)−Fe2(z^2) interaction maximizes for γ = 90°. We conclude that the weak exchange-coupling in $[Fe_2(O_2)(OBz)_2\{HB(pz')_3\}_2]$ (J = −33 cm^{-1}) primarily reflects the general efficiency of the cis μ-1,2 peroxide bridge to mediate antiferromagnetic coupling in Fe(III) dimers rather than a specific structural feature. The lower effectiveness of the peroxide bridge relative to the oxo bridge in mediating antiferromagnetism will be addressed in the *Discussion*.

Spectral Assignments. The d → d transitions in octahedral high-spin ferric complexes are all spin forbidden and exhibit molar extinction coefficients ϵ in the range between 0.1 and 1.0 M^{-1} cm^{-1}.[45,46] On the basis of their high extinction coefficients, the five Gaussian resolved bands in the optical absorption and MCD spectra of $[Fe_2(O_2)(OBz)_2\{HB(pz')_3\}_2]$ (Figure 4 and Table 1) are thus readily assigned to ligand-to-metal CT transitions. The Raman profiles for the peroxide-related Fe−O and O−O stretching modes (Figure 2) indicate that bands 1−4, in contrast to band 5, are all associated with peroxide-to-iron CT transitions. For the assignment of band 5, a comparison with the absorption spectrum of the μ-hydroxo-bridged complex $[Fe_2OH(O_2CCH_3)_2\{HB(pz)_3\}_2]^+$ [47] is useful. In the visible and near-IR regions, the corresponding spectrum exhibits only weak bands with ϵ values <5 M^{-1} cm^{-1}. In contrast, intense features ($\epsilon \gg$ 1000 M^{-1} cm^{-1}) assigned to pyrazole-to-Fe and carboxylate-to-Fe CT transitions[47] occur in the UV with maxima above 27 500 cm^{-1} and tail into the visible. We conclude that band 5 in the spectra in Figure 4 arises from OBz-to-Fe and/or pyrazole-to-Fe CT transitions.

An important aspect of singly excited states in dimers is their two-fold degeneracy[48,49] that arises from the fact that either one

(44) A detailed theoretical and spectroscopic study of μ-oxo-bridged diiron(III) complexes is presented in ref 32. However, to facilitate comparison with the peroxide models, the calculations were repeated using the ADF program version 2.0.1.

(45) Lehmann, G. *Z. Phys. Chem. Neue Folge* **1970**, *72*, 279.

(46) Lever, A. B. P. *Inorganic Electronic Spectroscopy*, 2nd ed.; Elsevier Science: Amsterdam, 1984; Chapter 6.

(47) Turowski, P. N.; Armstrong, W. H.; Liu, S.; Brown, S. N.; Lippard, S. J. *Inorg. Chem.* **1994**, *3*, 636.

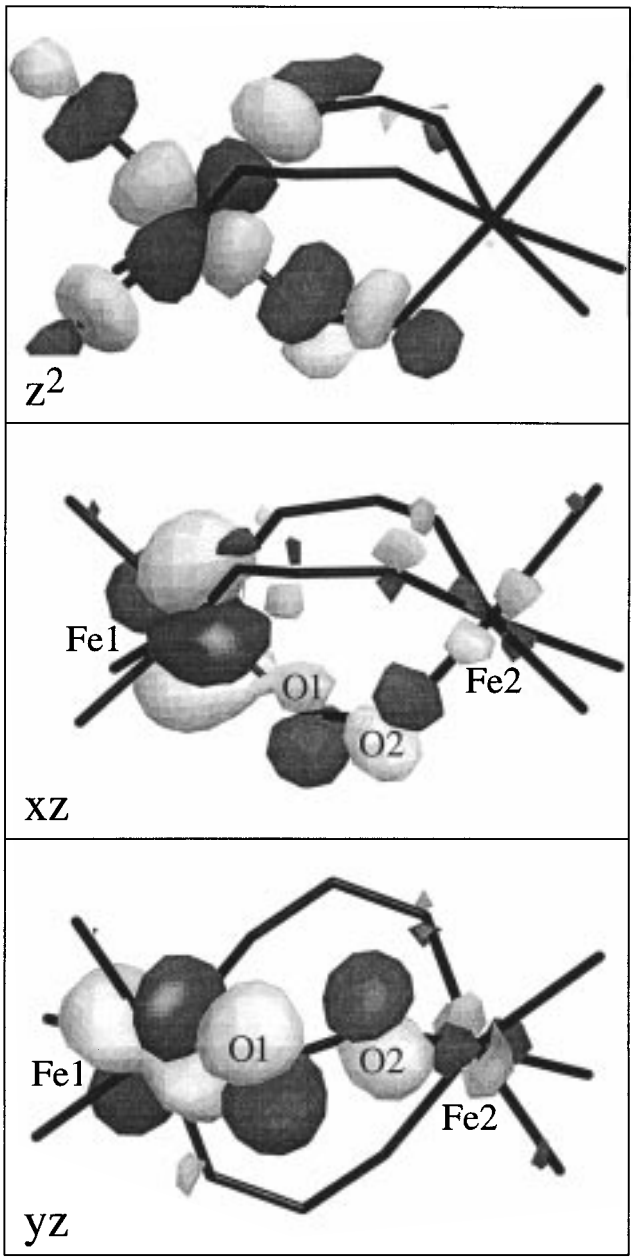

Figure 8. Surface plots of the relevant Fe1 d-based unoccupied spin-down MOs obtained from a BS calculation on $[Fe_2(O_2)(O_2CH)_2(NH_3)_6]^{2+}$.

of the two metal ions can be excited. The locally excited configurations are not eigenfunctions of the dimer Hamiltonian, and the proper wave functions are given by the symmetric and antisymmetric combinations of these configurations. The HS wave functions, in contrast to the BS wave functions, do have proper dimer symmetry and, given the weak exchange interactions in the ground and excited states of $[Fe_2(O_2)(OBz)_2\{HB(pz')_3\}_2]$, it is reasonable to use the results from the HS calculation in the following analysis of the peroxide-to-Fe CT transitions.

Calculations have shown that the intensities of CT transitions can be approximated by a sum of overlaps of individual ligand orbital contributions in the corresponding donor and acceptor MOs.[50] Thus, the MO compositions obtained from the HS calculation on $[Fe_2(O_2)(O_2CH)_2(NH_3)_6]^{2+}$ greatly assist in the assignments of the peroxide-to-Fe CT bands. By inspection of Table 2 it is noted that only two of the Fe d-based MOs have a high peroxide character; that is, levels 28a [$yz(+)$ mixed with π_π^*] and 29b [$z^2(-)$ mixed with π_σ^*]. The two dominant peroxide-to-Fe CT bands in the absorption spectrum of $[Fe_2(O_2)(OBz)_2\{HB(pz')_3\}_2]$ (Figure 4) are thus assigned to $\pi_\pi^* \rightarrow yz(+)$ (band 2) and $\pi_\sigma^* \rightarrow z^2(-)$ (band 4), indicated by arrows in the energy level diagram of Figure 5. The surface plots of the corresponding donor and acceptor orbitals (Figure 7) provide insight into the different resonance Raman enhancement behavior of ν(Fe−O) and ν(O−O) for excitation within bands 2 and 4 (Figure 2). The $\pi_\pi^* \rightarrow yz(+)$ transition strongly affects the Fe−O bond: it formally eliminates the π-bonding interaction. This gives rise to comparable enhancement of the ν(Fe−O) and ν(O−O) modes, indicating that the excited state is mainly distorted along the Fe−O stretching coordinate[51] (vide infra). Upon $\pi_\sigma^* \rightarrow z^2(-)$ excitation, on the other hand, significant electron density is removed from the peroxide π_σ^* orbital, leading to a substantially stronger O−O bond in the excited state and thus predominant enhancement of ν(O−O) in the resonance Raman spectrum.

The MCD activity of $[Fe_2(O_2)(OBz)_2\{HB(pz')_3\}_2]$ arises from Boltzmann population differences in Zeeman split sublevels of the ground state and is thus typical of *C*-term behavior. Expansion of the *C*-term MCD intensity expression yields a sum of three contributions, each of which will vanish as orbital degeneracies are lifted unless some mechanism exists for mixing polarizations.[52,53] Spin-orbit coupling between two excited states gives rise to two perpendicular transition moments of the transitions to the coupled states, thus providing a mechanism for MCD intensity in complexes of low symmetry. In this case, the sum of the MCD intensities over the two spin-orbit-coupled excited states vanishes, which would lead to characteristic derivative-shaped pseudo-*A*-term features, as observed in the MCD spectra of $[Fe_2(O_2)(OBz)_2\{HB(pz')_3\}_2]$ in Figures 3 and 4 (note that the crossover of bands 3,4 is displaced from zero intensity due to the paramagnetic impurity).

In the approximate C_2 symmetry, both the $\pi_\pi^* \rightarrow yz(+)$ and $\pi_\sigma^* \rightarrow z^2(-)$ transitions are polarized along the C_2 (**z′**) axis. The two pseudo-*A*-term features comprising bands 1,2 and bands 3,4, respectively, thus indicate that the transitions associated with bands 1 and 3 are polarized perpendicular to **z′**. Because of its weakness and large number of possible assignments, we do not attempt here to assign band 1 to a specific peroxide-to-Fe CT transition. The high absorption intensity of band 3 and its close vicinity to band 4 indicate that the corresponding transition is either $\pi_\sigma^* \rightarrow z^2(+)$ or $\pi_\pi^* \rightarrow z^2(-)$, because both the symmetric and antisymmetric combinations of the Fe *xy* orbitals have practically no peroxide character (Table 2). The two possible assignments for band 3 can be evaluated on the basis of the Raman profiles in Figure 2. The $z^2(+)$ orbital has only little peroxide character (Table 2), part of which is σ bonding, and promotion of an electron from peroxide π_σ^* to $z^2(+)$ should result in a large distortion along the O−O coordinate and therefore preferentially enhance ν(O−O). In contrast, the $z^2(-)$ orbital is substantially mixed with π_σ^*, and the $\pi_\pi^* \rightarrow z^2(-)$ transition should primarily enhance ν(Fe−O). Thus, the strong

(48) Eickman, N. C.; Himmelwright, R. S.; Solomon, E. I. *Proc. Natl. Acad. Sci. U.S.A.* **1979**, *76*, 2094.

(49) Güdel, H. U.; Weihe, H. In *Molecular Magnetism: From Molecular Assemblies to the Devices;* Coronado, E.; et al., Eds.; Kluwer Academic: Netherlands, 1996; pp 173−197.

(50) (a) Ros, P.; Schuit, G. C. A. *Theor. Chim. Acta (Berlin)* **1966**, *4*, 1. (b) Van der Avoird, A.; Ros, P. *Theor. Chim. Acta (Berlin)* **1966**, *4*, 13.

(51) The relative displacement Δ of an excited state along a resonance enhanced mode can be estimated from the Raman intensity: $I \propto \Delta^2 \nu^2$.

(52) Gerstman, B. S.; Brill, A. S. *J. Chem. Phys.* **1985**, *82*, 1212.

(53) Gewirth, A. A.; Solomon, E. I. *J. Am. Chem. Soc.* **1988**, *110*, 3811.

Table 6. Energies (eV) and Compositions (%) of the Relevant Fe1 Centered Unoccupied Spin-Down BS Orbitals and *J* Values Calculated for $[Fe_2(O_2)(O_2CH)_2(NH_3)_6]^{2+}$, Two Related Structures, and a μ-oxo-bridged Fe(III) Dimer[a]

	$\gamma = 129°, \tau = 53°$				$\gamma = 129°, \tau = 0°$				$\gamma = 120°, \tau = 0°$				μ-oxo dimer		
level	Fe1	O1	O2	Fe2	Fe1	O1	O2	Fe2	Fe1	O1	O2	Fe2	Fe1	O	Fe2
z^2	67	8	4	0	66	10	5	0	67	11	4	0	67	13	0
yz	61	22	10	3 z^2	67	22	8	1 yz	63	21	8	1 yz	79	16	1 yz
xz	79	5	4	3 z^2	72	6	6	5 z^2	63	4	6	10 z^2	53	22	14 z^2
J[b]		−128				−121				−143				−342	

[a] Total contributions from Fe d, O1,O2(peroxide) p, and O(oxo) p orbitals. [b] Calculated exchange-coupling constants in cm^{-1} ($H = -2J\mathbf{S}_1\mathbf{S}_2$).

Table 7. Comparison of Experimental and Calculated Transition Energies (cm^{-1})

band[a]	transition	pol[b]	obs	calc
2	$\pi_\pi^* \rightarrow yz(+)$	$\mathbf{z}'$	14 620	15 445
3	$\pi_\pi^* \rightarrow z^2(-)$	$\mathbf{x}',\mathbf{y}'$	24 650	24 445
	$\pi_\pi^* \rightarrow z^2(+)$	$\mathbf{z}'$		24 705
	$\pi_\sigma^* \rightarrow z^2(+)$	$\mathbf{x}',\mathbf{y}'$		26 585
4	$\pi_\sigma^* \rightarrow z^2(-)$	$\mathbf{z}'$	26 200	26 965

[a] Band designations relate to Figure 4 and Table 1. [b] Polarizations are given in the approximate C_2 point group.

enhancement of ν(Fe−O) relative to ν(O−O) (Figure 2) allows us to assign band 3 to $\pi_\pi^* \rightarrow z^2(-)$ which is polarized perpendicular to $\mathbf{z}'$, as required by the pseudo-*A*-term feature.

Because bands 4 and 3 are associated with electronic excitations from π_σ^* and π_π^*, respectively, to the same acceptor orbital, $z^2(-)$, their energy separation allows us to estimate the π_σ^*/π_π^* splitting, $\Delta(\pi_\sigma^* - \pi_\pi^*)$. Using the band positions from the better resolved toluene spectra (Figure 4, Table 1), a value for $\Delta(\pi_\sigma^* - \pi_\pi^*)$ of ∼1550 cm^{-1} is obtained, which is in good agreement with the calculated value of $\Delta(\pi_\sigma^* - \pi_\pi^*) = 1225$ cm^{-1} (Figure 5, Table 2).

For comparison, the energies of the transitions associated with bands 2−4 were calculated from the difference in total energy of the excited and ground states at convergence. The results are presented in Table 7. The correspondence between the experimental and calculated transition energies is excellent, which strongly supports the aforementioned assignments. The calculations can thus be used to obtain a reasonable estimate of the energies of the $\pi_\pi^* \rightarrow z^2(+)$ and $\pi_\sigma^* \rightarrow z^2(+)$ transitions (Table 7) that are not observed in absorption but could affect the Raman intensities in the UV region (vide infra).

Peroxide-to-Fe Charge Donation. In this section, the CT absorption and Raman data shown in Figure 2 are used to obtain quantitative experimental estimates of the σ and π donor strengths of peroxide in $[Fe_2(O_2)(OBz)_2\{HB(pz'_3\}_2]$. In general, the donor strength of a given ligand can be related to the integrated intensities of all the CT transitions associated with this ligand.[38] Because bonding interactions between peroxide and Fe primarily involve the peroxide π^* and Fe d orbitals,[54] the peroxide-to-Fe CT bands in the absorption spectrum of Figure 4 permit a good estimate of the charge donation by peroxide to Fe in $[Fe_2(O_2)(OBz)_2\{HB(pz'_3\}_2]$.

Using the formalism of Baldwin et al.,[38] the contribution from each of the half-occupied iron d orbitals, d_i, to the peroxide π^* orbitals is approximately given by

$$(C_{\pi^*}^{d_i})^2 = \kappa \frac{f_i}{\nu_i |\mathbf{r}|^2} \qquad (3)$$

where κ is a constant (9.22×10^{-2} Å), f_i and ν_i are the oscillator strength and transition energy of the peroxide-to-Fe(d_i) CT transition, respectively, and $\mathbf{r}$ is the transition vector that coincides with the O(peroxide)−Fe bond vector in $[Fe_2(O_2)(OBz)_2\{HB(pz'_3\}_2]$. The donor ability of peroxide corresponds to the total amount of Fe d character in the peroxide-based π^* orbitals, and eq 3 thus relates the charge donation by peroxide to the intensities of the peroxide-to-Fe CT transitions. The spectral assignments in Table 7 differentiate between transitions originating from π_π^* and π_σ^*, therefore allowing us to separate π and σ donor interactions. However, this requires that we quantitate the absorption intensity associated with the peroxide-to-Fe CT transitions relative to other contributions in the UV region.

The weak Raman enhancement of the peroxide-related ν(Fe−O) and ν(O−O) modes in the UV region (Figure 2) suggests that only part of the observed absorption intensity above 25 000 cm^{-1} is associated with peroxide-to-Fe CT transitions. Using the resonance Raman intensities to quantitate this contribution is complicated for two reasons. First, the close vicinity of bands 3 and 4 (Figure 4) indicates that the corresponding electronic states can interact, which would give rise to constructive and destructive interference, leading to large and unexpected changes in the Raman intensities.[55] Second, the variation of the ν(Fe−O)/ν(O−O) resonance Raman intensity ratio as a function of the excitation wavelength shows that each of the three excited states associated with bands 2−4 exhibits different distortions along these modes.

This two-mode/three-states problem is ideally suited for an analysis within the framework of time-dependent theory of electronic absorption and resonance Raman spectroscopy.[56] In this formalism, the absorption spectrum for an electronic transition to an excited state r is given by[57]

$$I(\nu) \propto \nu \int_{-\infty}^{\infty} \langle \phi | \phi(t) \rangle_r \exp[i\nu t]\, dt \qquad (4)$$

where $I(\nu)$ is the absorption intensity at energy ν. If it is assumed that the ground- and excited-state vibrational frequencies are identical and that the normal modes are not mixed in the excited states, then the wave packet overlap $\langle \phi | \phi(t) \rangle_r$ takes the form

$$\langle \phi | \phi(t) \rangle_r = \exp\left[\sum_n \left(-\frac{\Delta_{n,r}^{\,2}}{2}(1 - \exp(-i\nu_n t)) - \frac{i\nu_n t}{2} \right) - iE_{0,r}\, t - \Gamma_r^{\,2} t^2 \right] \qquad (5)$$

where ν_n is the vibrational frequency of the nth normal mode and $\Delta_{n,r}$ is the dimensionless displacement of state r relative to the ground state along mode n. The parameter $E_{0,r}$ is the energy of the zero-phonon transition to state r and Γ_r is a damping factor that governs the resolution of the vibrational structure.

(54) Contributions from the Fe 4s and 4p orbitals are <1%.

(55) Wootton, J. L.; Zink, J. I. *J. Am. Chem. Soc.* **1997**, *119*, 1895.

(56) Myers, A. B.; Mathies, R. A. In *Biological Applications of Raman Spectroscopy*; Spiro, T. G., Ed.; Wiley: New York, 1987; Vol. 2, pp 1−58.

(57) Tannor, D. J.; Heller, E. J. *J. Chem. Phys.* **1982**, *77*, 202.

To simulate a spectrum with several overlapping absorption bands, the full spectrum can be expanded in terms of a sum of individual spectra calculated with eq 4.

In the low-temperature limit, the Raman polarizability of a system with k electronic excited states can be written as a half-Fourier transform

$$\alpha_{i\rightarrow f}(\nu_l) = \frac{i}{\hbar}\int_0^\infty \left(\sum_{r=1}^{k} {\mu_r}^2 \langle\phi_f|\phi(t)\rangle_r \exp[-iE_{0,r}t - \Gamma_r t]\right) \times \exp[i\nu_l t]\, dt \quad (6)$$

where μ_r is the transition dipole moment for the electronic transition from the ground state to the excited state r ($\mu_r^2 \propto f_r$) and ν_l is the energy of the incident laser radiation. The time-dependent overlap is given by

$$\langle\phi_f|\phi(t)\rangle_r = \prod_n \left\{ \exp\left[-\frac{{\Delta_{n,r}}^2}{2}(1 - \exp[-i\nu_n t]) - \frac{i\nu_n t}{2}\right] \times (1 - \exp[-i\nu_n t])^{q_n} \frac{(-1)^{q_n}{\Delta_{n,r}}^{q_n}}{(2^{q_n} q_n!)^{1/2}} \right\} \quad (7)$$

where ϕ_f is the final vibrational level of the electronic ground state. This level differs from the vibrational ground state, corresponding to the initial state in the Raman process (low-temperature limit), by q_n quanta in normal mode n. The intensity of the Raman transition $i \rightarrow f$ is then obtained from

$$I_{i\rightarrow f} \propto \nu_l {\nu_s}^3 |\alpha_{i\rightarrow f}|^2 \quad (8)$$

where ν_s is the energy of the scattered radiation. For example, the Raman profile for the fundamental of normal mode m is obtained from eqs 6−8 with $q_{n\neq m} = 0$ and $q_{n=m} = 1$.

In the present case, the analysis involves three excited states, corresponding to bands 2−4 in Figure 4, and two normal modes, ν(Fe−O) and ν(O−O). To include the information derived from the MCD data, we required that each of the three simulated absorption spectra reproduces the relative intensities, peak maxima, and widths of one of the Gaussian resolved bands 2−4 in Figure 4. This allowed us to place severe constraints on the values of μ^2, Δ, and E_0. The signs of the dimensionless displacements Δ were assigned on the basis of the orbital compositions obtained from the electronic structure calculations (see *Nature of the Fe-Peroxide Bond*): Δ(Fe−O) > 0 (elongation of the Fe−O bond) and Δ(O−O) < 0 (contraction of the O−O bond) for each excited state. Further, a value of Γ_r = 500 cm^{-1}, typical of transition metal complexes,[58] was assigned to each damping factor. A direct modeling approach, as described by Myers et al.,[56] was then used to search for the complete parameter set that generates the best simultaneous fit to the experimental 77 K glass absorption and resonance Raman data (Figure 2). The refined parameters are given in Table 8.

In Figure 9A, the simulated absorption spectrum, obtained from a sum of the three individual spectra calculated with the fitted parameters in Table 8 (bands 2−4) and Gaussian bands 1 and 5 from Figure 4, is superimposed on the 77 K glass absorption spectrum. The corresponding Raman profiles of ν(Fe−O) and ν(O−O) for bands 2−4, scaled for best correspondence with the experimental data in the visible spectral region, are shown in Figure 9B. Below 21 000 cm^{-1}, the agreement is excellent, whereas in the UV region, the calculated Raman intensities are significantly higher than those observed experimentally. Given the good correspondence in the visible region, the parameters in Table 8 can be used to estimate the overtone-to-fundamental intensity ratio for ν(Fe−O) to verify our tentative assignment of the Raman feature at 832 cm^{-1} to 2ν(Fe−O). The calculated ratio of ∼0.3 agrees well with the experimental value of ∼0.25, lending support to our assignment.

There are several possible sources of the weak Raman enhancement in the UV region: (i) Both the $\pi_\pi^* \rightarrow z^2(+)$ and $\pi_\sigma^* \rightarrow z^2(+)$ transitions could also contribute to the observed absorption intensity in this region (Table 7). Because the resonance Raman intensity of a given mode n is roughly proportional to the square of the absorption intensity and ${\Delta_n}^2$, the presence of more than two, accordingly weaker and sharper bands in the UV range would greatly reduce the resonance Raman enhancement in this region. (ii) The π_π^*, $\pi_\sigma^* \rightarrow z^2(+)$ excited states are sufficiently close in energy to the π_π^*, $\pi_\sigma^* \rightarrow z^2(-)$ excited states corresponding to bands 3 and 4 to cause resonance deenhancement. (iii) Only part of the absorption intensity above 20 000 cm^{-1} is associated with peroxide-to-Fe CT transitions, as might be anticipated from the presence of

Table 8. Excited-State Parameters from Simultaneous Fit to the Absorption and Resonance Raman Data of Figure 4[a]

band	E_0, cm^{-1}	Δ(Fe−O)	Δ(O−O)	${\mu_{ref}}^{2}$ [b]
2	10 000	3.68	−1.98	1.00
3	20 150	4.39	−1.20	0.24
4	21 600	2.95	−2.55	0.60

[a] Obtained with eqs 4−8 and Γ_r = 500 cm^{-1}, ν(Fe−O) = 421 cm^{-1}, and ν(O−O) = 876 cm^{-1}. [b] Obtained with $\mu^2 \propto f/\nu_{max}$ and the parameters of Table 1.

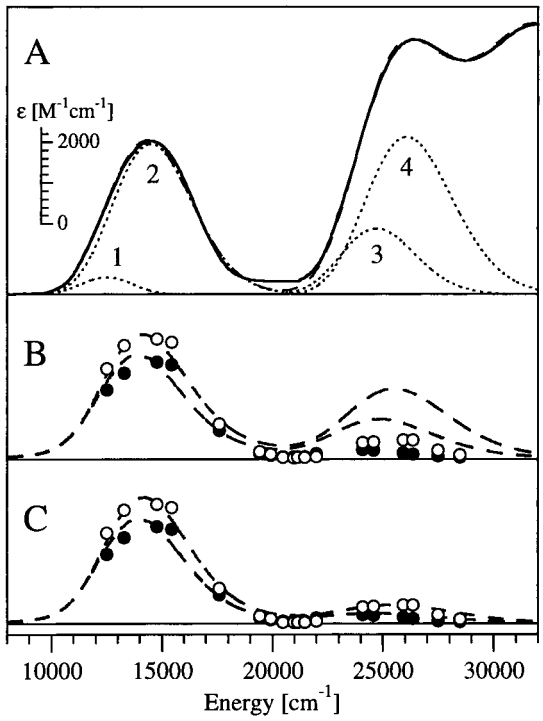

Figure 9. (A) 77 K absorption spectrum of [Fe₂(O₂)(OBz)₂{HB(pz′)₃}₂] in a toluene glass (solid line) and simulated spectrum (broken line), obtained from a sum of bands 2−4 calculated with the fitted parameters in Table 8 and the Gaussian absorption bands 1 and 5 (not shown) from Figure 4. (B) Corresponding experimental resonance Raman excitation profiles for the ν(Fe−O) (●) and ν(O−O) (○) fundamental bands and simulated profiles for bands 2−4 (broken lines), scaled for best correspondence in the visible region. (C) As in B, except that the simulated profile was calculated with bands 3 and 4 scaled to 55%.

(58) Zink, J. I.; Shin, K. S. K. *Adv. Photochem.* **1991**, *16*, 119.

intense UV absorption bands in the optical spectrum of $[Fe_2OH(O_2CCH_3)_2\{HB(pz)_3\}_2]^+$ that tail into the visible region.[47]

The Gaussian bands 1−4 in Figure 4 thus represent an upper limit of the peroxide-to-Fe CT absorption intensity. A lower limit is obtained, in any case, by assuming that contribution (iii) is solely responsible for the weak Raman enhancement in the UV region. The intensities of bands 3 and 4 were therefore varied by floating the corresponding values of μ_r^2 in eq 6 for the best fit to the experimental Raman profiles over the full spectral range. The simulated Raman profiles, obtained with bands 3 and 4 scaled to 55% according to the fitted scaling factor, are compared with the experimental data in Figure 9C. The correspondence is very satisfactory, and we conclude that bands 1 and 2, together with bands 3 and 4 scaled to 55%, provide a reasonable lower limit of the peroxide-to-Fe CT absorption intensity in $[Fe_2(O_2)(OBz)_2\{HB(pz')_3\}_2]$.

Having determined upper and lower limits for the peroxide-to-Fe CT transition intensity, we can now estimate the peroxide → Fe donor strength in $[Fe_2(O_2)(OBz)_2\{HB(pz')_3\}_2]$ for the two limiting cases using eq 3. The absolute values are not expected to be quantitatively accurate, but this method allows us to compare the relative π and σ donor interactions and provides a useful measure for a comparison with the known series of Cu−peroxide complexes[38] (see *Discussion*). Because the $z^2(-)$ orbital has σ-bonding interactions with both peroxide π^* orbitals, bands 3 and 4 (and we assume band 1) reflect the σ and band 2 the π donor interactions. Using eq 3, the parameters in Table 1, and $|\mathbf{r}| = r(\text{Fe}-\text{O}) = 1.885$ Å, we estimate that the π contribution to the donor strength by peroxide lies between 50% and (with bands 3 and 4 scaled to 55%) 65%. These numbers agree well with the computational results that also suggest that the π donor interaction is dominant (Tables 2 and 3).

Excited-State Distortions. The major feature in the absorption spectrum of $[Fe_2(O_2)(OBz)_2\{HB(pz')_3\}_2]$ is the prominent band in the visible region (band 2 in Figure 4) assigned to the $\pi_\pi^* \rightarrow yz(+)$ peroxide-to-Fe CT transition (Table 7). Because this feature is characteristic of all cis μ-1,2 peroxide-bridged Fe(III) dimers, it serves as their spectral fingerprint[3] and can play an important role in the detection of Fe−peroxide intermediates in the catalytic cycle of non-heme iron enzymes.[10] The boundary surface plots of the π_π^* donor and $yz(+)$ acceptor orbitals (Figure 7) indicate that this transition formally eliminates the Fe−peroxide π-bonding interaction. Thus, an excited-state distortion analysis was undertaken to obtain further information about the relative strength of the peroxide−Fe π-bonding interaction in $[Fe_2(O_2)(OBz)_2\{HB(pz')_3\}_2]$.

The excited-state distortion can be expressed in terms of internal coordinates using the eigenvectors obtained from the NCA (see *Normal Coordinate Analysis*, Table 5) and the dimensionless displacements from the quantitative Raman analysis (see *Peroxide-to-Fe Charge Donation*, Table 8). The internal coordinate changes, Δr_i (Å), are related to normal coordinate displacements, Δ_n, by[56]

$$\Delta r_i = 5.8065 \sum_n L_{i,n} \frac{\Delta_n}{\sqrt{\nu_n}} \qquad (9)$$

where $L_{i,n}$ is the ith element of the mass-weighted eigenvector, $\mathbf{L}_n$, for the nth normal mode. A schematic illustration of the nuclear distortions of the $Fe_2(O_2)$ core accompanying the $\pi_\pi^* \rightarrow yz(+)$ transition is shown in Chart 2 (top).

Because the signs of the displacements Δ are ambiguous in the harmonic approximation, there are three other phase combinations of the distortions along ν(Fe−O) and ν(O−O) in addition to the one shown in Chart 2. Therefore, the geometry of the $Fe_2(O_2)$ four-atom core, with the remainder of the $[Fe_2(O_2)(O_2CH)_2(NH_3)_6]^{2+}$ model kept frozen, was optimized using ADF calculations in both the ground and $\pi_\pi^* \rightarrow yz(+)$ excited states. The computationally optimized geometries are shown in Chart 2, bottom. The correspondence with the experimentally determined structures (Chart 2, top) is good, lending justification to the choice of phase combination in Chart 2.

Chart 2. Experimental and Calculated Ground and $\pi_\pi^* \rightarrow yz(+)$ Excited State Geometries of the $Fe_2(O_2)$ Core

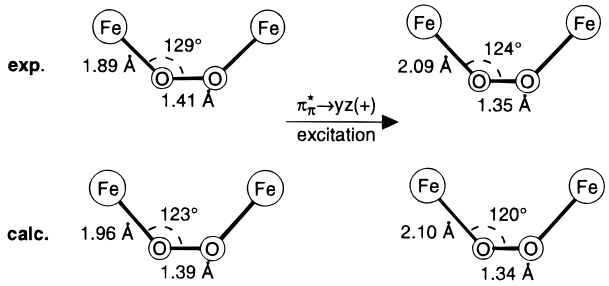

As expected from the orbital plots in Figure 7, the major distortion in the $\pi_\pi^* \rightarrow yz(+)$ excited state occurs along the Fe−O bonds, whereas the O−O bond is less affected. The O−O bond length of 1.35 Å in the excited state is typical of superoxide[18] and reflects the CT character of this transition. The Fe−O bond length change of $\Delta r_{\text{Fe}-\text{O}} = 0.20$ Å is substantial and unusually large for a low-energy CT excitation. This demonstrates the importance of the π-bonding interaction between Fe and peroxide in $[Fe_2(O_2)(OBz)_2\{HB(pz')_3\}_2]$ because the presence of a dominant σ-bonding interaction would greatly reduce the distortion along the Fe−O coordinate. The large distortions accompanying the $\pi_\pi^* \rightarrow yz(+)$ transition also provide some insight into the high photoinstability of $[Fe_2(O_2)(OBz)_2\{HB(pz')_3\}_2]$. From Chart 2 we would expect that the excited state may decay by release of O_2. This corresponds to a photoinduced deoxygenation process and was observed for some Co(III)−peroxide complexes.[59]

Discussion

The interaction of binuclear non-heme Fe(III) proteins with dioxygen has been the subject of much recent work in bioinorganic chemistry.[2,3] However, surprisingly little is known about the nature of Fe−peroxide bonding in cis μ-1,2 peroxide-bridged Fe(III) dimers, although this bridging mode has been proposed for the putative peroxide intermediate *P* of MMO.[10] In contrast, previous spectroscopic[38] and theoretical studies[60] of a series of Cu(II)−peroxide complexes exhibiting several binding modes of peroxide provided significant insight into Cu−peroxide bonding. A comparison of the results obtained here with parallel data reported for the Cu complexes is presented next.

Comparison of Fe−Peroxide and Cu−Peroxide Bonding. In Cu−peroxide complexes, the bonding interaction between Cu(II) and peroxide involves the peroxide π^* orbitals and the single half-occupied Cu d orbital.[60] The π_σ^* orbital is oriented in the Cu−O−O plane and is stabilized by a strong σ donor interaction with copper. The other π^* orbital, π_v^* (designated π_π^* in $[Fe_2(O_2)(OBz)_2\{HB(pz')_3\}_2]$ because it now participates in π bonding), is oriented vertical to the Cu−O−O plane and

(59) Maecke, H. R.; Williams, A. F. In *Photoinduced Electron Transfer*; Fox, M. A., Chanon, M., Eds.; Elsevier: Amsterdam, 1988; Part D, p 28.
(60) Ross, P. K.; Solomon, E. I. *J. Am. Chem. Soc.* **1991**, *113*, 3246.

Table 9. Comparison of Peroxide−Metal Bonding in $[Fe_2(O_2)(OBz)_2\{HB(pz')_3\}_2]$ and Three Cu(II)−Peroxide Complexes[a]

complex	$\sum f_i$	$\sum(f_i/\nu_i)^b$	$(C_{\pi^*}^M)^2$	k_{O-O}	ν_{O-O}
Fe cis μ-1,2[c]	0.183 (0.135)	944 (760)	1.8 (1.4)	3.1	876
Cu end-on monomer	0.105	537	1.0	2.9	803
Cu trans μ-1,2	0.252	1350	1.9	3.1	832
Cu side-on μ-η^2:η^2	0.479	1730	3.7	2.4	763

[a] f_i (ν_i) is the oscillator strength (peak position) of the ith peroxide-to-metal CT transition, $(C_{\pi^*}^M)^2$ is the relative charge donation by peroxide, and k_{O-O} and ν_{O-O} are the force constant (mdyn/Å) and frequency (cm^{-1}), respectively, of the O−O stretching mode ν(O−O). Data for the series of Cu complexes were taken from ref 38. [b] In Å units. [c] The two parameter sets represent upper (lower) limits (see text).

exhibits only weak π interactions with occupied Cu d orbitals. From the intensities of the peroxide-to-Cu CT transitions, a ratio of 1:1.9:3.7, or ∼1:1:2 per Cu, was derived for the relative charge donation by peroxide to Cu in an end-on monomer, a trans μ-1,2 dimer, and a side-on μ-η^2:η^2 dimer.[38] Thus, a roughly linear increase is observed in the relative charge donation with increasing number of peroxide−Cu σ-bonding interactions. A comparison of the results for the series of Cu complexes and those obtained for $[Fe_2(O_2)(OBz)_2\{HB(pz')_3\}_2]$ is given in Table 9. Despite the strong π-bonding interaction, the charge donation by peroxide in $[Fe_2(O_2)(OBz)_2\{HB(pz')_3\}_2]$ is not greater than in the trans μ-1,2 Cu dimer, and the bridging peroxide can thus be considered as equally negative in the two complexes. Hence, a similarly strong O−O bond would be expected in these dimers, because electron density is primarily removed from the π^* orbitals that are antibonding with respect to the O−O bond.

The O−O bond strength is reflected in the O−O force constant k_{O-O}, and the corresponding values obtained from NCAs of the vibrational data of $[Fe_2(O_2)(OBz)_2\{HB(pz')_3\}_2]$ and the three Cu−peroxide complexes[38] are included in Table 9. As expected, the O−O bond is equally strong in the μ-1,2 peroxide-bridged Fe and Cu dimers and stronger than in the end-on Cu monomer, reflecting the higher electron density in the antibonding peroxide π^* orbitals of the monomer. Note, however, that the side-on Cu dimer with four strong Cu−peroxide σ-bonding interactions exhibits the lowest O−O stretching frequency because in this dimer the unoccupied peroxide σ^* orbital acts as a π acceptor.[60]

Table 9 shows that the O−O stretching frequencies for the μ-1,2 peroxide-bridged Fe and Cu dimers differ substantially, although the O−O force constants are identical. The key to an understanding of this result is provided by Figure 6B, which shows a plot of the O−O stretching frequency as a function of the metal−O−O bond angle γ, calculated using a Urey−Bradly force field and the set of refined force constants for $[Fe_2(O_2)(OBz)_2\{HB(pz')_3\}_2]$. From $\gamma = 90°$ to 140°, the frequency increases from 815 to 901 cm^{-1} because of mechanical coupling between the metal−O and O−O stretch motions. In the trans μ-1,2 copper complex, the Cu−O−O angle is 108°,[17] and mechanical coupling is thus unimportant. In contrast, in the Fe dimer γ equals 129° (based on the structure of the phenylacetate analog[16]) and ν(O−O) involves 18% Fe−O stretch motion (Table 5). As a consequence, the effective reduced mass is greatly lowered, leading to the high observed O−O stretching frequency for $[Fe_2(O_2)(OBz)_2\{HB(pz')_3\}_2]$. Note that this coupling is not apparent from the $^{16}O_2 \rightarrow {}^{18}O_2$ isotope shifts (Figure 6B, bottom) because the Fe−O stretch also primarily involves oxygen motion.

In μ-1,2 peroxide-bridged dimers an interesting correlation is found between the metal−O−O bond angle γ and the nature of the metal−peroxide bonding interaction. In Cu(II) and Co(III) dimers, the corresponding angles are similar to each other, that is, 108° for the end-on trans copper dimer[17] and 112° averaged for a total of 22 cis and trans Co dimers (covering a range between 109 and 118°).[18,61,62] Both Cu(II)[60] and low-spin Co(III)[63] have a fully occupied t_{2g} set of d orbitals in these complexes, and only σ-bonding interactions with the peroxide π_σ^* orbital contribute to the net bonding. Reorientation of the corresponding O(peroxide) p orbitals would require mixing with the unoccupied σ^* orbital, which is much higher in energy. Thus, intraperoxide bonding places severe constraints on the metal−O−O angle in Cu− and Co−peroxide dimers; a value of $\gamma \sim 110°$ appears to maximize the σ-bonding interaction. A different situation exists in cis μ-1,2 peroxide-bridged Fe dimers where the Fe−O−O angles in the three structurally characterized complexes are 120°,[14] 123°,[15] and 129°.[16] The strong π-bonding interaction between Fe and peroxide involves half-occupied Fe d orbitals and thus effectively contributes to the net bonding. This interaction is fairly independent of the Fe−O−O bond angle γ and thus allows for more structural flexibility: while a smaller angle permits better σ-bonding interaction, a larger Fe−O−O angle is favored for steric and electrostatic reasons. A comparison of the structures of $[Fe_2(Ph\text{-}bimp)(OBz)(O_2)]^{2+}$ [14] and $[Co_2(bimp)(OBz)(O_2)]^{2+}$ [62] is interesting. Given the fairly rigid bridging skeleton, the metal−metal distances are not permitted to differ by much; that is, Fe···Fe = 3.33 Å and Co···Co = 3.15 Å. However, the metal−O−O angles are substantially different: 120° and 110°, respectively. The small Co−O−O angle in the Co dimer is accomplished by a large Co−O−O−Co dihedral angle of $\tau = 51°$, as compared with $\tau = 10°$ in the Fe complex. There exist a number of cis μ-1,2 peroxide-bridged Co dimers for which the Co···Co separation is ∼3.3 Å,[62] similar to the Fe···Fe separation in $[Fe_2(Ph\text{-}bimp)(OBz)(O_2)]^{2+}$. Nevertheless, the Co−O−O bond angle is again ∼110° accomplished by an even larger dihedral angle of $\tau \sim 61°$. For comparison, in monobridged trans μ-1,2 cobalt dimers, where the monomeric units are permitted to rotate about the O−O bond, the Co−O−O−Co unit is ususally planar. This suggests that a large dihedral angle in the cis μ-1,2 Co dimers results from the dominance of the σ-bonding interaction that maximizes when γ is small.

The different nature of Fe−peroxide and Cu−peroxide bonding is reflected in the energy splitting of the peroxide π^* orbitals. Due to the large π contribution to the peroxide → Fe charge donation in $[Fe_2(O_2)(OBz)_2\{HB(pz')_3\}_2]$, antibonding electron density is shifted from the peroxide π_π^* orbital to the half-occupied Fe(yz) d orbitals, which are π bonding to peroxide (see Figure 7). This bonding interaction greatly reduces the energy of the π_π^*-based MO and leads to a small π_σ^*/π_π^* splitting of <2000 cm^{-1}. In Cu−peroxide complexes, the peroxide π_v^* orbital can only interact with fully occupied Cu d orbitals, and the π_v^*-based MO is thus primarily localized on peroxide.[60] As a result, the π_σ^*/π_v^* splitting is large; ∼4000 cm^{-1} observed and calculated for the end-on Cu monomer[60,64] and ∼10 000 cm^{-1} calculated for the trans μ-1,2 Cu dimer[60] where the experimental situation is complicated by strong antiferromagnetic exchange interactions in the CT excited states.[39]

(61) Barraclough, C. G.; Lawrance, G. A.; Lay, P. A. *Inorg. Chem.* **1978**, *17*, 3317.
(62) Kayatani, T.; Hayashi, Y.; Suzuki, M.; Uehara, A. *Bull. Chem. Soc. Jpn.* **1994**, *67*, 2980.
(63) Tuczek, F.; Solomon, E. I. *Inorg. Chem.* **1992**, *31*, 944.
(64) Pate, J. E.; Cruse, R. W.; Karlin, K. D.; Solomon, E. I. *J. Am. Chem. Soc.* **1987**, *109*, 2624.

Chart 3. Proposed Mechanism for the Conversion of *P* to a High-Valent Diiron(IV)−Oxo Species

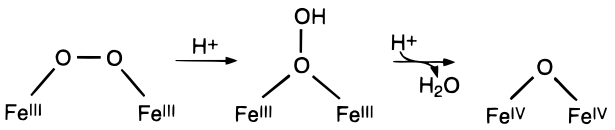

Mechanistic Implications. In reactivity studies it was found that the trans μ-1,2 Cu dimer possesses a peroxide ligand that is relatively basic.[65] Thus, the similar charge donation by peroxide in this dimer and $[Fe_2(O_2)(OBz)_2\{HB(pz')_3\}_2]$ (Table 9) suggests that the bridging peroxide in the Fe complex also has a rather basic/nucleophilic character. This result has some important implications with respect to dioxygen activation by MMO and RR. The CD and MCD studies of reduced MMO[66] and RR[67] have indicated that there is an open coordination position on each Fe(II) and that both ferrous ions are capable of exogenous ligand binding. The initial steps in the reactions of MMO and RR with dioxygen involve the two-electron reduction of O_2 by the diferrous active site affording a peroxide-bridged diiron(III) intermediate and the subsequent cleavage of the peroxide O−O bond to form a high-valent Fe−oxo species.[2,3] Several binding modes for peroxide in the enzyme intermediates have been proposed, of which side-on μ-η^2:η^2 and cis μ-1,2 binding modes are considered to be the most likely.[3,12,19] Support for a side-on structure is provided by recent work on a binuclear Cu−peroxide model complex that shows reversible cleavage and formation of the O−O bond, thereby interconverting between a side-on peroxide and a di-μ-oxo core structure.[68] However, it is noted that the electronic structure of the side-on Cu complex is unique in that the unoccupied peroxide σ* orbital acts as a π acceptor, weakening the O−O bond.[60] Studies are underway to explore whether a similar π back-bonding interaction can occur in analogous side-on Fe(III) dimers.

On the basis of Mössbauer data[16] and supported by recent calculations,[20−22] a cis μ-1,2 bridging mode is currently favored for the peroxide intermediate *P* in MMO.[3,12,19] Given the rather nucleophilic character of the cis μ-1,2 bridging peroxide evaluated relative to the series of Cu−peroxide complexes, it would appear reasonable that protonation and heterolytic cleavage of the O−O bond could lead to a binuclear Fe(IV)−oxo species (Chart 3). This mechanism parallels the one proposed for the heme-containing monooxygenase cytochrome P-450, where heterolytic cleavage of peroxide produces an Fe(IV)═O porphyrin radical intermediate.[69,70] Support for this scheme is provided by recent spectroscopic and electronic structural studies of a hydroperoxo−copper model complex.[71] It was found that protonation activates the peroxide for further reduction by a large stabilization of the peroxide orbitals, including the unoccupied σ* orbital. Thus, in the case of MMO, protonation of the bridging peroxide would facilitate the conversion of *P* to a high-valent Fe−oxo species. Two-electron reduction is favored because it involves a large thermodynamic driving force that is required to overcome the large Franck−Condon barrier associated with reductive cleavage of the O−O bond.[72] Hence, in the reaction scheme in Chart 3, the second Fe of the active sites of MMO and RR fulfills the role of the porphyrin in supplying the second electron. This Fe serves the further role of providing a coordination site for the bridging peroxide that will be unstable toward formation of a μ-oxo bridge in a high-valent intermediate due to the high stability of the Fe−O(oxo) bond.[32] Alternatively, in Hr, a μ-oxo bridge is already present in the peroxide bound form (oxyHr), and hence this site is stable toward further oxidation. The fact that there is dominant His·N ligation in Hr,[4] in contrast to the oxygen-rich ligation in MMO[3] and RR,[5] could also contribute to the differences in reactivity of these sites.[73] For MMO, a mechanism for O−O bond cleavage by protonation of the bridging peroxide is also consistent with kinetic data for the decay of *P*. From the large activation entropy that indicates a transition state with increased degrees of freedom, it was concluded that the O−O bond cleavage may be accompanied by release of a water molecule.[74] Note that from $^{18}O_2$-labeling experiments it is known that the oxo bridge in the oxidized form of RR[75] and the oxygen in the hydroxylation product of MMO[3] derive from dioxygen, whereas the fate of the second oxygen has not yet been determined. Further studies will be required to fully understand the conversion from *P* to the putative Fe(IV)−oxo dimeric species.

Exchange Coupling. It is striking that the exchange-coupling constant in $[Fe_2(O_2)(OBz)_2\{HB(pz')_3\}_2]$ is only -33 cm^{-1} compared with $-J > 300$ cm^{-1} in μ-1,2 peroxide-bridged Cu dimers.[38,39,60] In homonuclear dimers with *n* half-filled orbitals on each metal center, *J* can be expressed in terms of a sum of individual contributions $J_{A_iB_j}$ as follows:[76]

$$J = \frac{1}{n^2}\sum_{i,j} J_{A_iB_j} \qquad (10)$$

where *A* and *B* refer to the two metal ions and *i* and *j* to their respective d orbitals. There are only a few of the 25 pathways in peroxide-bridged Fe(III) dimers that promote antiferromagnetism (Figure 8), and their contribution will be scaled by $1/n^2 = 1/25$ (eq 10). In binuclear Cu−peroxide complexes, the single ($n = 1$) superexchange pathway involves the half-occupied d orbital on each Cu atom that strongly interacts with the peroxide π_σ^* orbital,[60] leading to large antiferromagnetic coupling between the two coppers.

More insight into the effectiveness of μ-1,2 bridging peroxide in mediating antiferromagnetism between Fe(III) atoms is obtained from a comparison with the bent μ-oxo-bridged Fe(III) dimer. The experimental *J* values for $[Fe_2(O_2)(OBz)_2\{HB(pz')_3\}_2]$ and $[Fe_2O(OAc)_2(tmtacn)_2]^{2+}$ (Fe−O−Fe angle of 120°) are -33 and -120 cm^{-1}, respectively.[23,77] From our

(65) Fox, S.; Karlin, K. D. In *Active Oxygen in Biochemistry*; Valentine, J. S., Foote, C. S., Greenberg, A., Liebman, J. F., Eds.; Blackie Academic & Professional: Glasgow, 1995; pp 188−231.
(66) Pulver, S.; Froland, W. A.; Fox, B. G.; Lipscomb, J. D.; Solomon, E. I. *J. Am. Chem. Soc.* **1993**, *115*, 12409.
(67) Pulver, S. C.; Tong, W. H.; Bollinger, J. M.; Stubbe, J.; Solomon, E. I. *J. Am. Chem. Soc.* **1995**, *117*, 12664.
(68) Halfen, J. A.; Mahapatra, S.; Wilkinson, E. C.; Kaderli, S.; Young, V. G.; Que, L.; Zuberbühler, A.; Tolman, W. *Science* **1996**, *271*, 1397.
(69) Ortiz de Montellano, P. R. In *Cytochrome P-450 Structure, Mechanism, and Biochemistry*; Ortiz de Montellano, P. R., Ed.; Plenum: New York, 1986; pp 217−271.
(70) Sono, M.; Roach, M. P.; Coulter, E. D.; Dawson, J. H. *Chem. Rev.* **1996**, *96*, 2841.
(71) Root, D. E.; Karlin, K. D.; Solomon, E. I., unpublished material.
(72) Shin, W.; Sundaram, U. M.; Cole, J. L.; Zhang, H. H.; Hedman, B.; Hodgson, K. O.; Solomon, E. I. *J. Am. Chem. Soc.* **1996**, *118*, 3202.
(73) However, a series of membrane-bound monooxygenases and desaturases have recently been identified that appear to be rich in His·N ligation but still activate dioxygen (see Shanklin, J.; Achim, C.; Schmidt, H.; Fox, B. G.; Münck, E. *Proc. Natl. Acad. Sci. U.S.A.* **1997**, *94*, 2981).
(74) Liu, K. E.; Valentine, A. M.; Wang, D.; Huynh, B. H.; Edmondson, D. E.; Salifoglou, A.; Lippard, S. J. *J. Am. Chem. Soc.* **1995**, *117*, 10174.
(75) Ling, J.; Sahlin, M.; Sjöberg, B.-M.; Loehr, T. M.; Sanders-Loehr, J. *J. Biol. Chem.* **1994**, *269*, 5595.
(76) Ferguson, J.; Guggenheim, H. J.; Tanabe, Y. *J. Phys. Soc. Jpn.* **1966**, *21*, 692.

calculations on a series of three cis μ-1,2 peroxide-bridged Fe(III) models (Table 6), we conclude that J exhibits only a weak structural dependence. In good agreement with the experimental results, the calculations predict that the magnitude of J increases by a factor of ~3 in going to the μ-oxo-bridged dimer. Thus, a more detailed consideration of the computational results is appropriate. The compositions of the relevant Fe1-centered unoccupied MOs obtained from BS calculations for the three peroxide models and the μ-oxo-bridged dimer are given in Table 6.[44] The Fe2 and peroxide (O1,O2) or oxo (O) character in these MOs reflects their effectiveness as superexchange pathways to mediate antiferromagnetic coupling. Accordingly, the crossed pathway involving the xz orbital on Fe1 and the z^2 orbital on Fe2 makes the dominant contribution to the ground-state exchange-coupling in all four complexes [in the nonplanar peroxide structure, the absence of a mirror plane allows for a second, similarly effective crossed pathway; that is, Fe1(yz)−peroxide(π^*_π)−Fe2(z^2)].

The dominance of crossed superexchange pathways which was experimentally verified for bent μ-oxo-bridged dimers[32,78] can be understood as follows. In the antiferromagnetic ground state, spin polarization causes the occupied spin-down orbitals on Fe2 to be largely stabilized below their unoccupied counterparts on Fe1 (and conversely for the spin-up orbitals; see Figure S2). This effect greatly reduces delocalization of the Fe2-centered t_{2g} orbitals onto Fe1 (Table 6). The e_g orbitals on Fe2, however, are sufficiently destabilized by the ligand field to shift close in energy to the unoccupied t_{2g} orbitals on Fe1. In the planar structures, only the Fe1 xz orbital has proper symmetry and orientation to mix with the Fe2 z^2 and peroxide or oxo orbitals, leading to the dominance of the Fe1(xz)−oxo/peroxide−Fe2(z^2) superexchange pathway (Table 6). Note that this spin polarization effect on exchange-coupling is not accounted for in the model developed by Hay, Thibeault, and Hoffmann[79] to estimate the ground state J value of dimers.

The BS contour plots of the dominant superexchange pathways (i.e., Fe1 xz-based unoccupied spin-down MOs) for the planar peroxide model with $\gamma = 120°$ and the μ-oxo-bridged dimer are shown in Figure 10. Although the Fe2 z^2 character is similar in both cases, delocalization onto the bridging ligand is more pronounced in the oxo dimer than in the peroxide dimer (see also Table 6). This result indicates that the Fe−O(oxo) bond is more covalent than the Fe−O(peroxide) bond, which is reflected in the higher intensity of the oxo-to-Fe CT transitions[32] relative to the peroxide-to-Fe CT transitions. The difference in covalency arises from the higher charge on O(oxo) relative to O(peroxide), leading (i) to a shorter Fe−O bond [1.79 Å for Fe−O(oxo)[77] versus 1.89 Å for Fe−O(peroxide)[16]] that allows for better ligand−metal orbital overlap, and (ii) to a shift of the oxygen p orbitals to higher energy and thus closer to the Fe d orbitals. Figure 10 indicates that an additional factor will also contribute to the different effectiveness of the oxo and peroxide bridges in mediating exchange-coupling. In the μ-oxo-bridged dimer, the Fe1 xz orbital is π antibonding to an oxo p hybrid orbital, which is favorably oriented for σ-antibonding interaction with the Fe2 z^2 orbital, representing a mixed π/σ pathway. The oxo hybrid orbital is formed from a linear combination of the two initially degenerate p orbitals in the Fe−O−Fe plane. In the peroxide-bridged dimer, the major superexchange pathway has a similar, although slightly perturbed mixed π/σ character. In this case, reorientation of the peroxide orbitals by combining the in-plane p orbitals requires mixing between the σ^b and π^*_σ orbitals which are largely separated in energy. Thus, intraperoxide bonding opposes proper reorientation of the oxygen p orbitals for better interaction with the Fe d orbitals, producing an additional contribution to the weaker exchange-coupling in peroxide-bridged Fe(III) dimers relative to their oxo-bridged analogues.

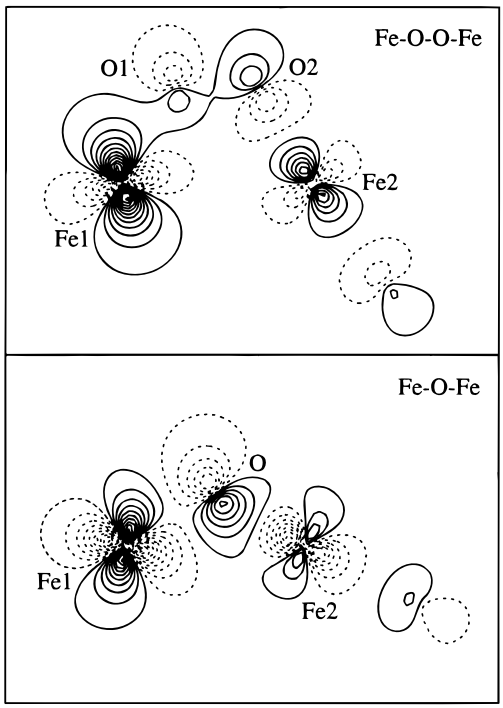

Figure 10. BS contour plots of the dominant superexchange pathways for a planar cis μ-1,2 peroxide-bridged model (top) and the μ-oxo-bridged analogue (bottom).

Summary and Conclusions

The π-bonding interaction between Fe and peroxide in μ-1,2 peroxide-bridged Fe(III) complexes makes a significant contribution to the Fe−peroxide bond. This interaction gives rise to larger metal−O−O angles in the three structurally characterized diiron(III)−peroxide complexes than in related Cu and Co complexes where the σ-bonding interaction makes the dominant contribution to the metal−peroxide bond. As a result, mechanical coupling between the Fe−O and O−O stretch motions becomes significant and the O−O stretching frequency becomes unusually high.

The similar charge donation by peroxide in [$Fe_2(O_2)(OBz)_2\{HB(pz')_3\}_2$] and the trans μ-1,2 peroxide-bridged Cu dimer suggests that the peroxide ligand in [$Fe_2(O_2)(OBz)_2\{HB(pz')_3\}_2$] should have a rather basic/nucleophilic character. Thus, provided a cis μ-1,2 binding mode occurs in the peroxide intermediates of MMO and RR, it would appear reasonable that protonation and heterolytic cleavage of the O−O bond could lead to the putative high-valent diiron(IV)−oxo species. It will now be important to extend these studies to other diiron(III)−peroxide structures and high-valent Fe−oxo intermediates to obtain molecular level insight into the mechanism of dioxygen activation by binuclear non-heme iron enzymes.

(77) Hartman, J. R.; Rardin, R. L.; Chaudhuri, P.; Pohl, K.; Wieghardt, K.; Nuber, B.; Weiss, J.; Papaefthymiou, G. C.; Frankel, R. B.; Lippard, S. J. *J. Am. Chem. Soc.* **1987**, *109*, 7387.

(78) Hotzelmann, R.; Wieghardt, K.; Flörke, U.; Haupt, H.-J.; Weatherburn, D. C.; Bonvoisin, J.; Blondin, G.; Girerd, J.-J. *J. Am. Chem. Soc.* **1992**, *114*, 1681.

(79) Hay, P. J.; Thibeault, J. C.; Hoffmann, R. *J. Am. Chem. Soc.* **1975**, *97*, 4884.

Acknowledgment. Financial support by the NSF-Biophysics Program Grant MCB 9316768 is gratefully acknowledged.

Supporting Information Available: Gaussian resolutions of the 55 K mull absorption and MCD spectra, energy level diagram from a BS calculation on $[Fe_2(O_2)(O_2CH)_2(NH_3)_6]^{2+}$, plots of the refined O−O force constant as a function of the Fe−O stretch and Fe−O−O bending force constants, table with the results from NCAs for $[Fe_2(O_2)(O_2CCH_2C_6H_5)_2\{HB(pz')_3\}_2]$ and $[Fe_2(O_2)(N\text{-Et-HPTB})(OBz)]^{2+}$, and tables reporting complete coordinates of all the models used for the calculations (9 pages, print/PDF). See any current masthead page for ordering information and Web access instructions.

JA980129X